Immersed boundary based near-wall modeling for large eddy simulation of turbulent wall-bounded flow

Shang-Gui Cai, Jérôme Jacob, Pierre Sagaut

Immersed boundary based near-wall modeling for large eddy simulation of turbulent wall-bounded flow

Shang-Gui Cai *, Jérôme Jacob, Pierre Sagaut

Aix Marseille Univ, CNRS, Centrale Marseille, M2P2 UMR 7340, Marseille 13451, France

ARTICLE INFO

Keywords:
Immersed boundary method
High Reynolds number
Large eddy simulation
Near-wall modeling

ABSTRACT

This paper describes the coupling of the immersed boundary method and the near-wall modeling of large eddy simulation for high Reynolds number turbulent flows over complex geometries on Cartesian grids. To overcome the spurious oscillation problem arising from the imposition of boundary conditions on the stair-case off-wall boundaries, several key ingredients have been employed, such as interpolating the friction velocity instead of the flow velocity from near-wall fluid interior points, evaluating the gradients by the weighted least square method and correcting the wall-normal gradient of the tangential velocity with the law of the wall at the off-wall boundaries. Furthermore, a hybrid RANS-LES approach has been applied to the near-wall eddy viscosity, either through an empirical blending function or the Reynolds stress balance constraint. We systematically discuss the effects of the hybrid eddy viscosity in a turbulent channel flow and a high lift three-element airfoil. Enforcing the Reynolds stress balance constraint turns out to be very robust in the considered cases. For the high lift three-element airfoil flow, the overall wall pressure and skin friction are predicted reasonably well and smoothly. The flow details are in a good agreement with the experimental data as well.

1. Introduction

The ever-increasing demand for handling complex or even moving boundaries more easily in numerical simulations boosts significantly the development of non-body fitting grid approaches, among which the immersed boundary method (IBM) is the most popular one. Initially proposed by Peskin in 1972 [1] for simulating flows over elastic boundaries, the IBM has been extensively explored in the past decades for a wide range of applications [2–5]. Without conforming to the boundary shapes, the grid generation is greatly simplified and becomes highly automatic, for instance the Cartesian grid which facilitates very simple and highly efficient discretization of flow equations such as the finite difference method, the lattice Boltzmann method, etc. The influence of the immersed boundaries on fluids is fulfilled by modifying the stencils close to wall (sharp interface IBM) [6–8] or by distributing an equivalent forcing term (diffuse interface IBM) [1,9–11].

The IBM has achieved a great success so far for low to moderate Reynolds number flows, however the application to high Reynolds number wall-bounded turbulent flows is very challenging. The primary reason is that the isotropic refinement of Cartesian grids leads to prohibitive grid numbers close to wall to resolve the thin turbulence boundary layer (TBL), much more excessive than the body-fitted counterpart as which can cluster the grids in the wall-normal direction. One remedy is to use wall models which replace the no-slip wall condition with highly refined grids by wall stress boundary condition with much coarser grids, under the assumption of constant shear stress close to wall. Even though the turbulence wall models have been well studied for body-fitted grids, the coupling to IBM is difficult since one has to apply the stress boundary condition on the off-wall boundaries. The sharp interface IBM is often considered superior to the diffuse interface IBM for this type of study [3]. In the sharp interface IBM the computational boundary lies on the off-wall grid surfaces which become stair-case when the immersed geometries are not aligned with the grid surfaces, always being the case for complex geometries. In these scenarios the distribution of the wall distance along the off-wall boundaries is highly oscillating. It is known that many wall models are sensitive to the wall distance even on body-fitted grids. The stair-case off-wall boundaries cause a lot of troubles in applying the turbulence wall model, among which one prominent issue is the spurious oscillations of the wall pressure and skin friction.

Numerous efforts have been devoted to smoothing the wall surface quantities. The fundamental problem lies in the fact that the near-wall coarse grids travel across different wall layers arbitrarily, resulting in large velocity variations between grid points that make the interpolation and gradient computation erroneous. To reduce large velocity gradients, Capizzano [12], followed by [13–15], suggested to

* Corresponding author.
E-mail address: shanggui.cai@univ-amu.fr (S.-G. Cai).

linearize the velocity profile artificially from a certain height down to the wall. The linearization approach is simple to implement but would potentially change the local flow behavior [16], as it violates the physical wall-law. Analogous to the body-fitted wall models based on adaptive grids [17], geometrical adaptation [18] or flow adaptation [19,20] techniques have been applied to the IBM based wall models by eliminating the grids too close to wall or shifting the off-wall boundaries outwards to reduce the velocity gradient, which turns out to be very effective in reducing the spurious oscillations. The off-wall boundary re-identification procedure inevitably introduces additional computation cost. Alternatively it was proposed in [16] to interpolate the friction velocity instead of the flow velocity, as the friction velocity is essentially insensitive to the wall distance. The velocity gradients, especially the wall-normal component for the shear stress condition, should be carefully treated in order to obtain smooth wall surface quantities [16]. The physical wall-law is thus respected and the original boundary grid layout can be maintained.

Aforementioned work has been dedicated to the Reynolds-averaged Navier–Stokes equations (RANS). Extending immersed boundary-wall modeling to the scale-resolving large eddy simulation (LES) gets more and more appealing nowadays owing to its inherent accuracy in predicting unsteady flows. Tessicini et al. [21] and Cristallo & Verzicco [22] employed the two-layer wall model of Balaras et al. [23] to prescribe the flow velocity or the shear stress on the off-wall boundaries. Further improvements have been made in [24–26] by modifying the near-wall eddy viscosity for correct imposition of the wall shear stress. Maeyama et al. [15] proposed to blend the eddy viscosity near-wall in IBM with a lattice Boltzmann solver. It is worth mentioning the body-fitted off-wall model, in which fluctuating velocities are prescribed at an artificially lifted wall. Problem arises immediately since the turbulent fluctuations at the lifted wall are not known *a priori*. The wall-normal velocity or transpiration velocity, on the other hand, is instantaneous at the lifted wall and has to satisfy the continuity constraint simultaneously. Jiménez and Vasco [27] have observed a strong sensitivity of the transpiration velocity to the flow. Further development can be found in [28–32]. As indicated by Bose & Park [33], it is practically difficult to identify the appropriate lifted location in case of complex geometries. This situation gets more complicated when combined with IBM as the wall distance is arbitrarily distributed along the off-wall boundary. The dynamic slip model [34,35] offered alternative way for imposing non-zero Reynolds stress at wall, in which the slip velocity boundary condition is formally derived from the filtered equations with the slip length computed dynamically using a Germano-like identity. The accuracy heavily depends on the dynamic procedure for the slip length, the subgrid models as well as the numerical methods [33]. The present work follows the hybrid RANS-LES approach and pursue smooth time-averaged wall surface quantities for general complex geometries with IBM.

The present paper is organized as follows. In Section 2 the LES governing equations and the flow solver are briefly described. In the following a fully explicit LES wall model consistent with the mixing length turbulence model is presented in Section 3. Section 4 describes the coupling of immersed boundary and LES near-wall modeling in detail. Numerical results are shown and discussed in Section 5, considering first the well known turbulent channel flow in Section 5.1 allowing for a fine validation of the present model and then the 30P30N three element airfoil in Section 5.2 to highlight the performance of the method for complex geometries. Finally conclusions are offered in Section 6.

2. Governing equations and numerical method

The filtered mass and momentum equations for compressible flows can be written as follows

$$\frac{\partial \bar{\rho}}{\partial t} + \frac{\partial \bar{\rho}\tilde{u}_i}{\partial x_i} = 0, \tag{1}$$

$$\frac{\partial \bar{\rho}\tilde{u}_i}{\partial t} + \frac{\partial}{\partial x_j}(\bar{\rho}\tilde{u}_i\tilde{u}_j) = -\frac{\partial \bar{p}}{\partial x_i} + \frac{\partial \tilde{\sigma}_{ij}}{\partial x_j} - \frac{\partial \tau_{ij}}{\partial x_j}, \tag{2}$$

with the Favre filtering given by $\tilde{u}_i = \overline{\rho u_i}/\bar{\rho}$, where u_i, ρ, p represent the fluid velocity, density and pressure respectively. $\tilde{\sigma}_{ij}$ is the viscous stress term

$$\tilde{\sigma}_{ij} = 2\bar{\rho}\nu\left(\tilde{S}_{ij} - \frac{1}{3}\tilde{S}_{kk}\delta_{ij}\right), \tag{3}$$

where ν is the molecular viscosity and δ_{ij} represents the Kronecker delta function. The resolved strain rate tensor is given by

$$\tilde{S}_{ij} = \frac{1}{2}\left(\frac{\partial \tilde{u}_i}{\partial x_j} + \frac{\partial \tilde{u}_j}{\partial x_i}\right). \tag{4}$$

The subgrid-scale (SGS) stress or residual stress arising from the filtering process is

$$\tau_{ij} = \bar{\rho}(\widetilde{u_i u_j} - \tilde{u}_i\tilde{u}_j). \tag{5}$$

Employing the eddy viscosity closure for the subgrid stress tensor leads to

$$\tau_{ij} = -2\bar{\rho}\nu_t^{\mathrm{LES}}\left(\tilde{S}_{ij} - \frac{1}{3}\tilde{S}_{kk}\delta_{ij}\right) + \frac{1}{3}\tau_{kk}\delta_{ij}. \tag{6}$$

The classical Smagorinsky model assumes that

$$\nu_t^{\mathrm{LES}} = (C_s\Delta)^2|\tilde{S}|, \quad |\tilde{S}| = \sqrt{2\tilde{S}_{ij}\tilde{S}_{ij}}, \tag{7}$$

where C_s is the Smagorinsky constant and Δ is the filter size which is usually taken as the grid size. The Smagorinsky model is found very dissipative close to wall, hence near-wall damping function is often employed to reduce the eddy viscosity, but theoretical justification is not clear. The dynamic Smagorinsky model [36,37] computes the constant dynamically using a test filter, provided the assumption that the constant is invariant between the two filtering levels. The computed constant however exhibits large oscillations which must be regularized for stability. In this work the subgrid model of Vreman [38] is used for the under-resolved eddies. It preserves the simplicity of the classical Smagorinsky model, using only the first-order velocity derivatives. Whereas it yields as good performance as the dynamic model but without explicit filtering or ensemble averaging in homogeneous directions. The Vreman's eddy viscosity on Cartesian grids is given by

$$\nu_t^{\mathrm{LES}} = C\Delta^2|\tilde{S}^*|, \quad |\tilde{S}^*| = \sqrt{\frac{B_\beta}{A_\beta}}, \tag{8}$$

where $C \approx 2.5C_s^2$. A_β and B_β are respectively the first invariant (trace) and the second invariant of the tensor $\boldsymbol{\beta}$ defined as

$$\boldsymbol{\beta} = \boldsymbol{\alpha}^{\mathrm{T}}\cdot\boldsymbol{\alpha} = \alpha_{ki}\alpha_{kj}, \quad \alpha_{ij} = \frac{\partial \tilde{u}_j}{\partial x_i}, \tag{9}$$

and

$$A_\beta = \mathrm{tr}(\boldsymbol{\beta}) = \|\boldsymbol{\alpha}\|^2 = \alpha_{ij}\alpha_{ij}, \tag{10}$$

$$B_\beta = \frac{1}{2}\left[(\mathrm{tr}(\boldsymbol{\beta}))^2 - \mathrm{tr}(\boldsymbol{\beta}^2)\right] = \beta_{11}\beta_{22} - \beta_{12}^2 + \beta_{11}\beta_{33} - \beta_{13}^2 + \beta_{22}\beta_{33} - \beta_{23}^2. \tag{11}$$

The lattice Boltzmann method (LBM) is employed in present work to solve the flow equations by evolving the mesoscopic particle distribution functions instead of the macroscopic variables. The macroscopic density and velocity are obtained by taking the moment of the particle distribution functions. The pressure is recovered by $p = \rho c_s^2$ with c_s being the speed of sound. Hence the LBM is often viewed as an artificial compressibility method for the weakly compressible low-Mach flows.

To enhance the stability at high Reynolds numbers, the hybrid recursive regularized density-based (HRR-ρ) LBM solver [39] is used along with the D3Q19 velocity sets, which is extensively validated in [14,16,18,39,40]. The stability is controlled by introducing a hyper-viscosity term that is turned on for the coefficient $0 \le \sigma_\nu < 1$ ($\sigma_\nu = 1$ corresponds to a null hyper-viscosity). In practical simulations, the

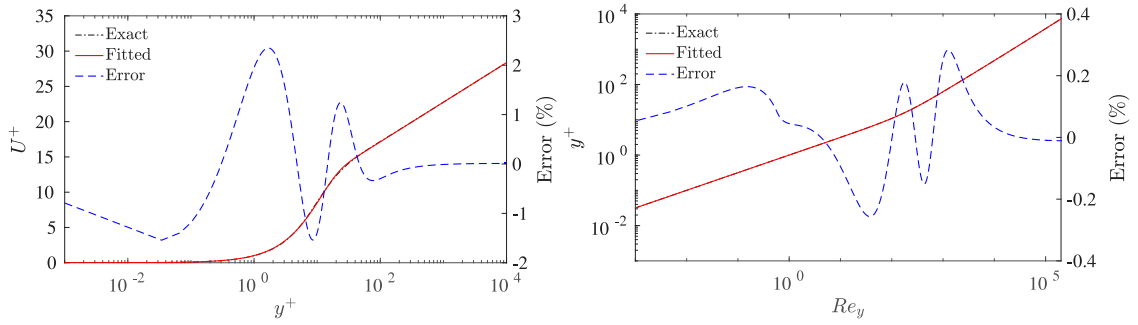

Fig. 1. Explicit wall model for the mixing length eddy viscosity model. (a) The velocity profile of U^+ as a function of y^+; (b) The inverse model with y^+ as a function of Re_y, where the Lambert W function (22) is truncated to the sixth order.

coefficient σ_ν is set to be slightly below one or can be computed dynamically [39].

Another crucial aspect of LBM is the specification of boundary conditions for the particle distribution functions as they have more degrees of freedom than the macroscopic variables. In this work, the particle distribution functions are totally reconstructed by the regularized finite-difference method [41], given the macroscopic boundary conditions of ρ, u_i, the sum of molecule viscosity ν and eddy viscosity ν_t, and the strain rate $\tilde{S}_{ij}$.

3. Explicit wall model for LES

When the near-wall grid is too coarse to support the LES modeling, the RANS model can be incorporated as a wall model to LES and provides it with a proper wall shear stress as boundary condition. Under the assumption of quasi-parallel flow close to wall without pressure gradient, the wall-normal integrated RANS momentum equation gives to the equilibrium wall model

$$\rho(\nu + \nu_t^{\mathrm{RANS}})\frac{dU}{dy} = \tau_w \equiv \rho u_\tau^2, \tag{12}$$

where $U \equiv \langle u \rangle$ represents the Reynolds averaged wall-tangential velocity and y is the wall-normal distance. It implies that the total shear stresses are equal to the wall shear stress τ_w near wall, with u_τ being the friction velocity. The equilibrium wall model can be expressed in viscous wall unit as

$$(1 + \nu_t^{\mathrm{RANS},+})\frac{dU^+}{dy^+} = 1, \tag{13}$$

with $U^+ = U/u_\tau$, $y^+ = yu_\tau/\nu$ and $\nu_t^{\mathrm{RANS},+} = \nu_t^{\mathrm{RANS}}/\nu$. The simple mixing length eddy viscosity model with near-wall damping is employed for closure, which is given by

$$\nu_t^{\mathrm{RANS},+} = \kappa y^+(1 - e^{-y^+/A^+})^2, \tag{14}$$

where $\kappa = 0.41$ and $A^+ = 19$.

The velocity profile can be obtained by integrating equation (13)

$$U^+ = \int \frac{1}{1 + \nu_t^{\mathrm{RANS},+}} dy^+, \tag{15}$$

whereas it is difficult to find the analytical form with above mixing length eddy viscosity model. Hence we propose the following fitted expression for the velocity as follows

$$U^+ = \left[1 - \tanh(\frac{y^+}{10.71})\right]^{1.526} y^+ + \left[\tanh(\frac{y^+}{10.71})\right]^{1.526} \frac{1}{\kappa}\log(Ey^+), \quad E = 11.27 \tag{16}$$

which blends the linear-law and the log-law in order to obtain a unified profile that is consistent with the specified eddy viscosity model. The constants are fitted to the numerically integrated equation (15). The velocity profile is displayed in Fig. 1(a) over the range of $y^+ \in [10^{-3}, 10^4]$. The fitted profile (16) is almost superimposed on the exact Eq. (15). The error mainly manifests in the buffer region with the maximum error of about 2%. In the logarithmic layer, the error is reduced to 0.01%. Hence the proposed velocity profile (16) can be considered sufficiently accurate.

However inverting equation (16) for the friction velocity u_τ is not trivial. Newton iteration can be performed but it becomes quite expensive for large scale problems. Moreover the convergence of the Newton iteration highly depends on the initial guess. Following the work by Cai and Sagaut [40], an explicit wall model will be derived with respect to the friction velocity for the mixing length model. We first define the local Reynolds number as

$$Re_y = \frac{Uy}{\nu} = U^+y^+, \tag{17}$$

In the viscosity sublayer, we have

$$U^+ = y^+ = (Re_y)^{1/2}, \tag{18}$$

and in the logarithmic layer, it is easy to get

$$(\kappa E Re_y) = (Ey^+)\log(Ey^+). \tag{19}$$

Donating $x = \kappa E Re_y$ and $W = \log(Ey^+)$, the above log-law can be rewritten as

$$x = W(x)e^{W(x)} \tag{20}$$

where $W(x)$ is actually the Lambert W function, computed by

$$W(x) = \log(\frac{x}{W(x)}). \tag{21}$$

The explicit wall model can be obtained if the Lambert W function is approximated by series, such as

$$W(x) \approx \log(\frac{x}{\log(\frac{x}{\log(x)})}) = \log(x) - \log(\log(x) - \log(\log(x))), \tag{22}$$

and inserting into the definition $W = \log(Ey^+)$ gives to

$$y^+(Re_y) = \frac{1}{E}e^{W(\kappa E Re_y)}, \tag{23}$$

We again blend the two explicit profiles (18) and (23) and calibrate the constants as follows

$$y^+(Re_y) = \left[1 - \tanh(\frac{Re_y}{180.8})\right]^{0.789} (Re_y)^{1/2} + \left[\tanh(\frac{Re_y}{180.8})\right]^{0.789} \frac{1}{E}e^{W(\kappa E Re_y)}. \tag{24}$$

Its profile is shown in Fig. 1(b), where the maximum error in the blending region is below 0.3% and reduces to 0.01% in the logarithmic layer, which clearly demonstrates the accuracy of the sixth-order

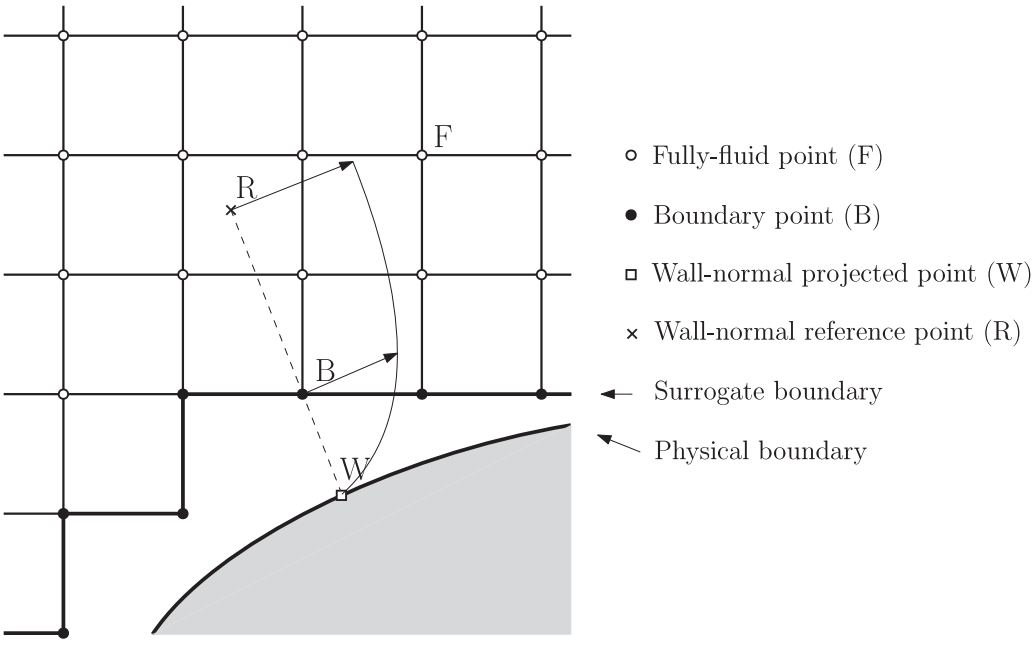

Fig. 2. Schematic of the immersed boundary and classification of grid points.

truncated Lambert W function for the traditional logarithmic law-of-the-law. Finally the friction velocity can be obtained straightforwardly by

$$u_\tau = y^+(Re_y)\nu/y. \tag{25}$$

4. Immersed boundary based LES near-wall modeling

4.1. Definition of computational boundary

The IBM adopts simple computational domain covered by Cartesian grids for flow simulation over complex geometries, which are represented by surface tessellations in current work. The wall effects can be incorporated either through a boundary force for the diffused interface IBM or a boundary reconstruction procedure for the sharp interface IBM. For high Reynolds number turbulent flows, the sharp interface IBM is usually preferred for better local accuracy.

A preliminary procedure for the boundary reconstruction is the identification of computational grid points, as shown in Fig. 2. The fluid points are declared as points lying entirely outside the immersed objects, which can be easily identified by the ray-tracing algorithm for example. The solid points can be defined conversely which however are not displayed in Fig. 2, since they are completely removed in current simulation. The fluid points can be further classified to boundary (non-fully-fluid) points and interior (fully-fluid) points. The boundary points are surrounded by at least one solid point, and they finally form the surrogate boundary of the flow domain for imposing the boundary conditions.

4.2. Near-wall interpolation

In the body-fitted WMLES, the LES equations are solved down to the wall, in which the RANS wall model is embedded into the LES domain from the wall to a modeling height, usually the first off-wall grid point. The wall model takes the instantaneous resolved velocity from LES as input at the modeling height and returns the shear stress to LES as boundary conditions at wall. In the immersed boundary simulation, the first off-wall grid point now becomes the surrogate boundary, but the second off-wall grid point does not necessarily in line with the first off-wall grid point in the wall-normal direction. Hence interpolation is required for obtaining information from LES in the wall-normal direction. A simple algorithm based on the inverse distance weighting is applied below [16]

$$\phi_R = \sum_k \omega_k \phi_k / q, \quad \omega_k = \left(\frac{1}{d_k}\right)^2, \quad q = \sum_l \left(\frac{1}{d_l}\right)^2, \tag{26}$$

where ϕ_R means generic quantities like $\tilde{u}_i$ or $\bar{\rho}$ at the reference point and d_k represents the Euclidean distance between the reference point and the donor point.

Kawai and Larsson [42] argued that it does not have to take the first off-wall grid point as the modeling height in body-fitted simulations, and suggested to use grid points far away from wall to improve the accuracy where the flow is well resolved by LES. In case of IBM, the choice of modeling height can be diverse and its location is crucial for accuracy. If it is too close to wall, the flow would not be well resolved by LES. If it is too far away from wall, the wall law may not be valid. Moreover the distribution of the modeling height is important for the wall surface quantities [16,19] in IBM. In [13,14] a fixed modeling height is selected. Preferably the modeling height should reside in the same wall layer with the donor point or at least above the viscous sublayer, such that the interpolation can be performed accurately [18–20]. Otherwise large spurious oscillations would occur near-wall and ruin the results dramatically. Cai et al. [16] presented a more general approach by which the friction velocity is first computed on each donor point using an explicit wall model and then interpolate the friction velocity to the boundary. Since the friction velocity is considered to be constant in wall-normal direction, the interpolation is performed only in the tangential direction. As a result, the ambiguous reference point is eliminated. It is found that the interpolation of the friction velocity is very accurate even on very coarse grids with low order interpolation method, such as the inverse distance weighting [16].

4.3. Boundary conditions of velocities and gradients

It is assumed that the tangential velocity follows exactly the wall-law profile, hence the tangential velocity at the boundary points can be determined from the wall model given the friction velocity. Since there is no universal law for the wall-normal velocity component, it is assumed to be zero in this study. Different treatment such as linear or quadratic approximations give negligible impacts on the results

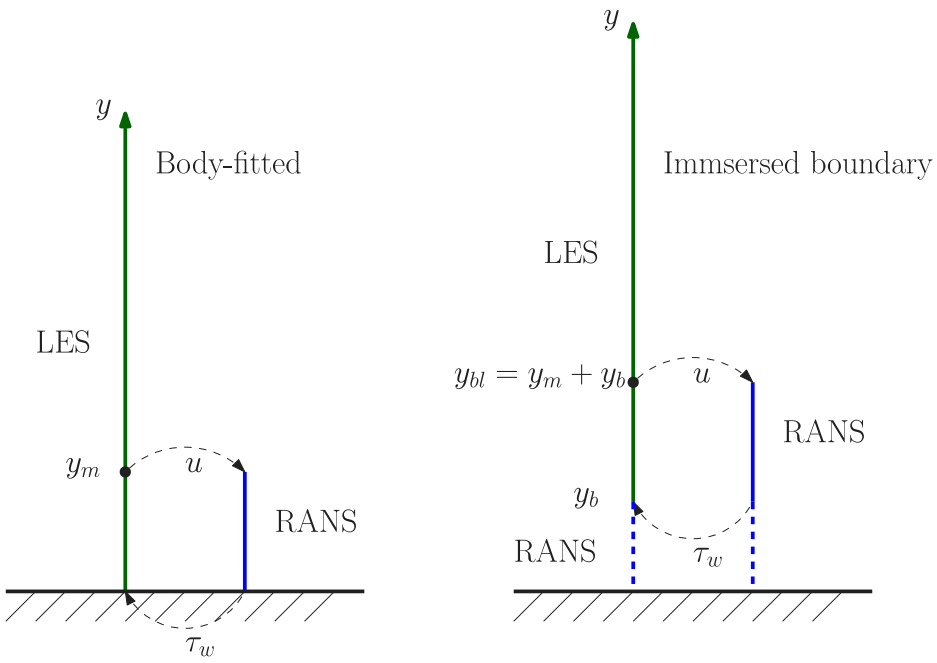

Fig. 3. LES near-wall modeling for the body-fitted grid and the immersed boundary grid.

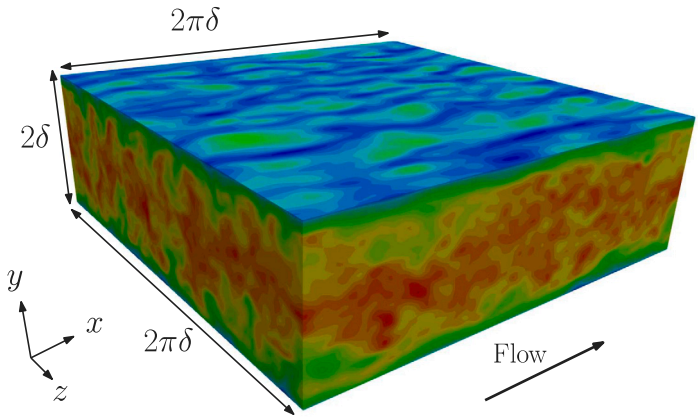

Fig. 4. Computational domain of the turbulent plane channel flow, where the contour shows the instantaneous velocity field on the fine grid.

in RANS [16]. Nevertheless prescribing only velocity values at the surrogate boundary is not sufficient, as a matter of fact the wall model indicates a stress boundary condition instead.

As the grid is too coarse to resolve the near-wall flow, the normal gradient would be considerably under-estimated, as well as the shear stress boundary condition. Therefore, the normal gradient is corrected from the wall-law profile. To do this, the velocity gradient tensor is first transformed into the wall-oriented coordinate

$$\mathbf{G}' = \mathbf{J} \cdot \mathbf{G} \cdot \mathbf{J}^{\mathrm{T}}, \tag{27}$$

where $\mathbf{G} = \nabla \mathbf{u}$ and

$$\mathbf{J} = \begin{bmatrix} s_x & s_y & s_z \\ n_x & n_y & n_z \\ t_x & t_y & t_z \end{bmatrix}, \tag{28}$$

where s, n, t represent the streamwise, wall-normal and span-wise directions respectively. To account for discrete effects, the finite-difference approximated wall-law gradient is employed for reconstructing the normal gradient in this work [16,18]. After correction, the velocity gradient tensor is transformed back into the Cartesian system by

$$\mathbf{G} = \mathbf{J}^{\mathrm{T}} \cdot \mathbf{G}' \cdot \mathbf{J}. \tag{29}$$

Caution should be taken to the other gradient components as well. The stair-case surrogate boundary degrades the centered finite-difference to one-sided finite-difference when one grid neighbor point is missing in that direction. This degeneration of accuracy order for gradient evaluation would be harmful to the skin friction. It is suggested in [13,16] to use more elaborate gradient scheme at the stair-case boundary, such as the weighted least square (WLSQ) method. The WLSQ gradient scheme minimizes the velocity error among the neighbor points

$$\mathbf{e} = \boldsymbol{\phi} - [\boldsymbol{\phi}_B + \mathbf{D} \cdot (\nabla \phi)_B], \tag{30}$$

where $\phi = u_i$, $\boldsymbol{\phi} = [\phi_1, \phi_2, \ldots, \phi_{n_b}]$ and $\mathbf{D} = [\mathbf{d}_1, \mathbf{d}_2, \ldots, \mathbf{d}_{n_b}]^{\mathrm{T}}$ with n_b being the number of neighbor points. The error function is defined as

$$J = \mathbf{e}^{\mathrm{T}} \mathbf{W} \mathbf{e}, \tag{31}$$

where inverse distance is used as the weight $\mathbf{W} = \mathrm{diag}(\omega_1, \omega_2, \ldots, \omega_{n_b})$. Taking $\partial J / \partial \mathbf{e} = 0$ gives to

$$(\nabla \phi)_B = (\mathbf{D}^{\mathrm{T}} \mathbf{W} \mathbf{D})^{-1} \mathbf{D}^{\mathrm{T}} \mathbf{W} (\boldsymbol{\phi} - \boldsymbol{\phi}_B). \tag{32}$$

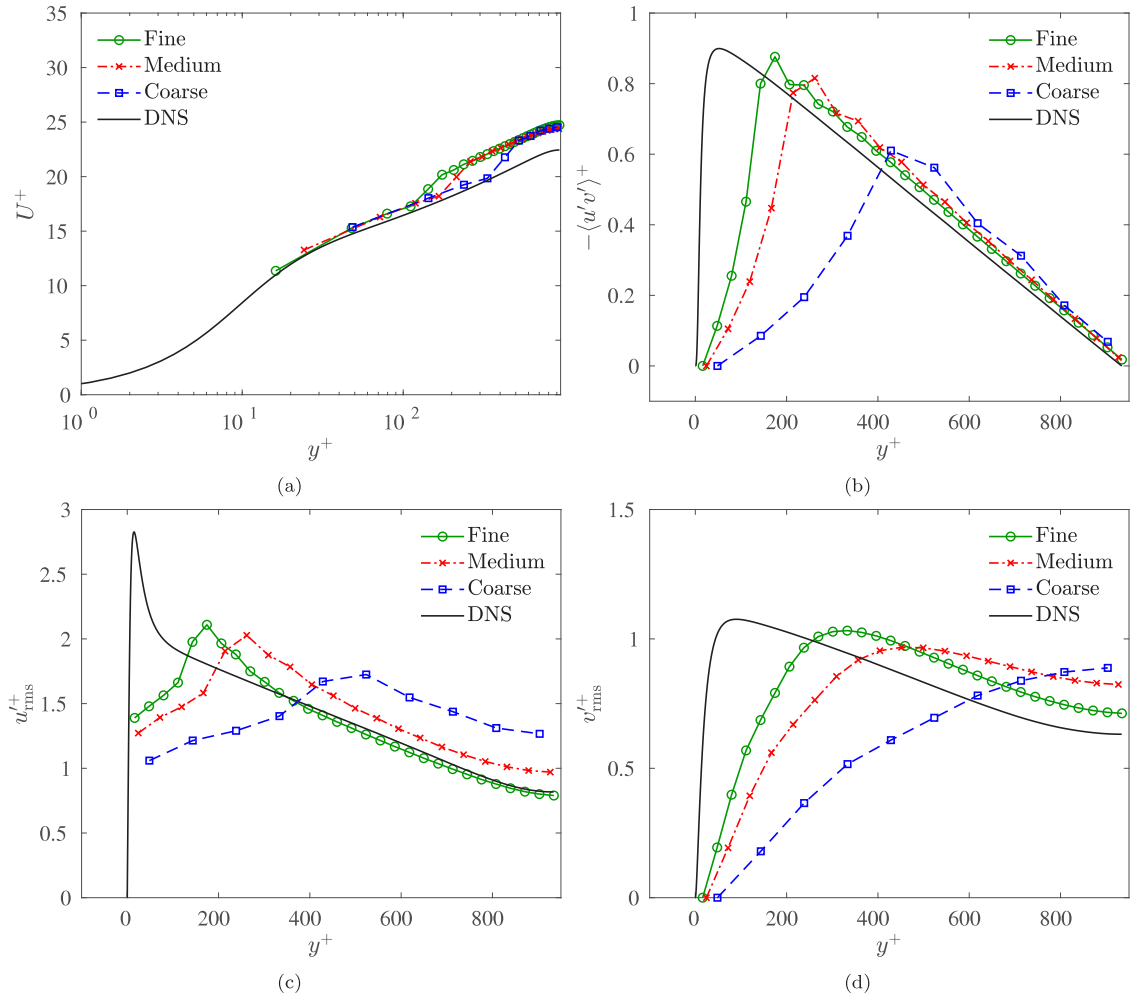

Fig. 5. Grid study of the turbulent channel flow at $Re_\tau = 950$ using the simplified constrained model. (a) The mean streamwise velocity U; (b) the resolved Reynolds stress $-\langle u'v'\rangle^+ = -\langle u'v'\rangle/u_\tau^2$; (c) the rms of the streamwise velocity $u'^+_{\mathrm{rms}} = u'_{\mathrm{rms}}/u_\tau$; (d) the rms of the normal velocity $v'^+_{\mathrm{rms}} = v'_{\mathrm{rms}}/u_\tau$.

The system can be solved analytically for all the velocity gradient components. It should be noted that the normal gradient reconstruction is performed after the WLSQ gradient scheme.

4.4. Near-wall eddy viscosity

As opposed to body-fitted grids, the IBM based WMLES is not solved down to the wall but to a finite height away from wall y_b, as illustrated in Fig. 3. The actual flow velocities are fluctuating and the Reynolds stress does not vanish at that height. Correctly prescribing turbulent fluctuations at the off-wall surrogate boundary turns out to be very difficult [27]. When the RANS wall shear stress is specified at the surrogate boundary, the simulation could be viewed as a kind of hybrid RANS-LES with the surrogate boundary as the zonal interface, except that the wall-normal grids are not refined to resolve the steep velocity gradient.

Without special treatment the current IBM using local reconstruction is not conservative for both mass and momentum. It was observed in [43] that the results are highly sensitive to the wall distance of the surrogate boundary. The stress loss becomes significant as the surrogate boundary is shifted away from the wall surface even on aligning grids in current simulations. This contradicts the requirement of reducing large velocity gradients by shifting the surrogate boundary away from wall. Furthermore, since coarse grids are used in the near-wall region, large numerical and SGS modeling errors will be occurred on the near-wall few grid points. The near-wall eddy viscosity model thus should compensate not only the under-resolved eddies but also all these deficiencies for a correct level of the Reynolds stress.

Enforcing the Reynolds stress constraint in the near-wall region has been extensively investigated in the body-fitted LES near-wall modeling, such as in WMLES [44–48] and in hybrid RANS-LES [15,49–52]. By dropping out the density for the specific stresses in weakly compressible flows, the balance of the Reynolds stress states that

$$R_{ij} = R_{ij}^{\mathrm{LES}} + \langle \tau_{ij} \rangle, \tag{33}$$

where $R_{ij}^{\mathrm{LES}} = \langle \tilde{u}_i \tilde{u}_j \rangle - \langle \tilde{u}_i \rangle \langle \tilde{u}_j \rangle$ is the resolved Reynolds stress by LES. The above balance equation (33) holds under the ergodic flow assumption, namely $\langle \tilde{\phi} \rangle = \langle \phi \rangle$ for a generic flow field, such that

$$\begin{aligned} R_{ij}^{\mathrm{LES}} + \langle \tau_{ij} \rangle &= \langle \tilde{u}_i \tilde{u}_j \rangle - \langle \tilde{u}_i \rangle \langle \tilde{u}_j \rangle + \langle \widetilde{u_i u_j} \rangle - \langle \tilde{u}_i \tilde{u}_j \rangle \\ &= \langle u_i u_j \rangle - \langle u_i \rangle \langle u_j \rangle \\ &= R_{ij}, \end{aligned} \tag{34}$$

where the true Reynolds stress R_{ij} can be approximated by a RANS model. Chen et al. [53] have observed no significant differences between the mixing length turbulence model and the Spalart–Allmaras turbulence model for the Reynolds stress constraint, in the test cases of turbulent channel flow and turbulent flow over a circular cylinder. In current work, we adopt the mixing length model for simplicity. As for the time-averaging, the exponentially weighted moving average [54] can be employed

$$\langle u_i \rangle^{n+1} = (1 - C_{\mathrm{exp}}) \langle u_i \rangle^n + C_{\mathrm{exp}} \tilde{u}_i^{n+1}, \tag{35}$$

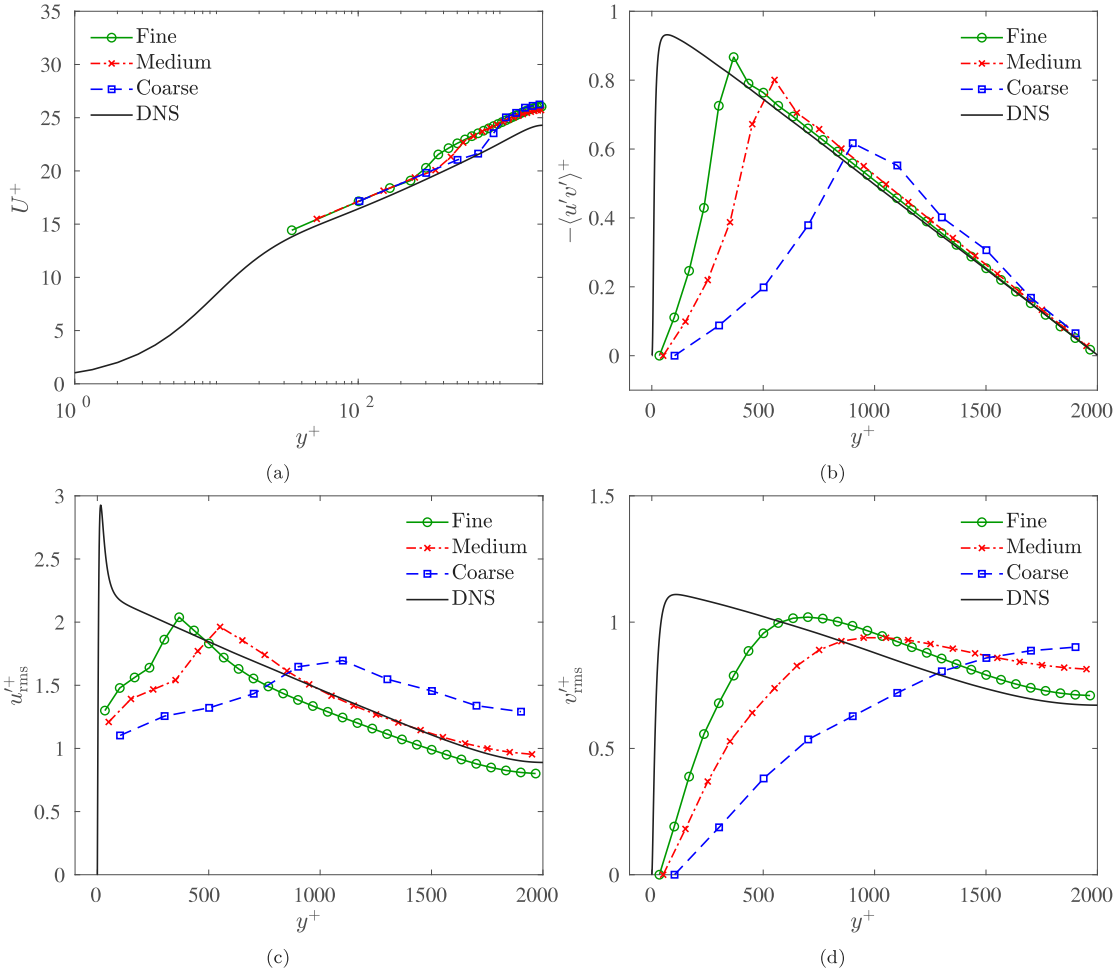

Fig. 6. Grid study of the turbulent channel flow at $Re_\tau = 2000$ using the simplified constrained model. (a) The mean streamwise velocity U; (b) the resolved Reynolds stress $-\langle u'v'\rangle^+ = -\langle u'v'\rangle/u_\tau^2$; (c) the rms of the streamwise velocity $u'^+_{rms} = u'_{rms}/u_\tau$; (d) the rms of the normal velocity $v'^+_{rms} = v'_{rms}/u_\tau$.

with

$$C_{\exp} = 3.628 f_c \Delta t, \tag{36}$$

where f_c is the cutoff frequency and Δt the time step. In current lattice Boltzmann method, the physical time step is determined by the grid size $\Delta t = \Delta x/(\sqrt{3}c_0)$ with c_0 being the sound speed. Averaging in homogeneous directions is preferable but it is generally not feasible for complex geometries.

There are many ways to fulfill the Reynolds-stress constraint in the near-wall region. In present work, we focus on the eddy viscosity closure for LES and RANS, hence the hybrid eddy viscosity can be easily defined as

$$\nu_t^{\text{hybrid}} = \beta \nu_t^{\text{LES}} + (1-\beta)\nu_t^{\text{RANS}}, \tag{37}$$

where $\beta \in [0,1]$ is the blending function to be specified.

- Empirical blending model

Kawai and Larsson [42,46] have presented a linear blending function in the body-fitted WMLES as follows

$$\beta = 1 - K^\gamma, \quad K = \max\left[\min(\frac{y_{bl}-y}{y_{bl}-y_c}, 1), 0\right], \quad y_c = \alpha y_{bl}, \tag{38}$$

with $\gamma = 1$ and $y_{bl} = y_m$. When applied to IBM based LES near-wall modeling [15], y_{bl} represents the blending height above which the turbulent flow is supposed to be well resolved by LES hence no blending action is undertaken. y_c denotes the starting height of blending below which the turbulence scales are all modeled by RANS. The eddy viscosity blending only acts in the intermediate region ($y_c \le y \le y_{bl}$). The parameter α ($0 \le \alpha \le 1$) which controls the blending region is prescribed to 0.36 in [42,46]. Maeyama et al. [15] have studied the sensitivity of these parameters in the turbulent channel flow and found best results with $\gamma = 2$ and $\alpha = 0.4$. Apparently the optimal parameters may vary for different problems and the Reynolds stress constraint (33) would not be strictly verified.

- Dynamic blending model

Applying the Reynolds stress constraint (33) to the eddy viscosity blending (37) gives to

$$\begin{aligned} -2\nu_t^{\text{RANS}}\langle\tilde{S}_{ij}\rangle &= R_{ij}^{\text{LES}} - 2\langle\nu_t^{\text{hybrid}}\tilde{S}_{ij}\rangle \\ &= R_{ij}^{\text{LES}} - 2\beta\langle\nu_t^{\text{LES}}\tilde{S}_{ij}\rangle - 2\nu_t^{\text{RANS}}\langle\tilde{S}_{ij}\rangle + 2\beta\nu_t^{\text{RANS}}\langle\tilde{S}_{ij}\rangle, \end{aligned} \tag{39}$$

that is,

$$\beta\left[2\langle\nu_t^{\text{LES}}\tilde{S}_{ij}\rangle - 2\nu_t^{\text{RANS}}\langle\tilde{S}_{ij}\rangle\right] = R_{ij}^{\text{LES}}, \tag{40}$$

where the blending function can be obtained by least square minimization

$$\beta = \frac{R_{ij}^{\text{LES}}\langle\tilde{S}_{ij}\rangle}{2\langle\nu_t^{\text{LES}}\tilde{S}_{ij}\rangle\langle\tilde{S}_{ij}\rangle - 2\nu_t^{\text{RANS}}\langle\tilde{S}_{ij}\rangle\langle\tilde{S}_{ij}\rangle}, \tag{41}$$

or

$$\beta = \frac{R_{ij}^{\text{LES}}\langle\tilde{S}_{ij}\rangle}{R_{ij}\langle\tilde{S}_{ij}\rangle - \langle\tau_{ij}\rangle\langle\tilde{S}_{ij}\rangle}. \tag{42}$$

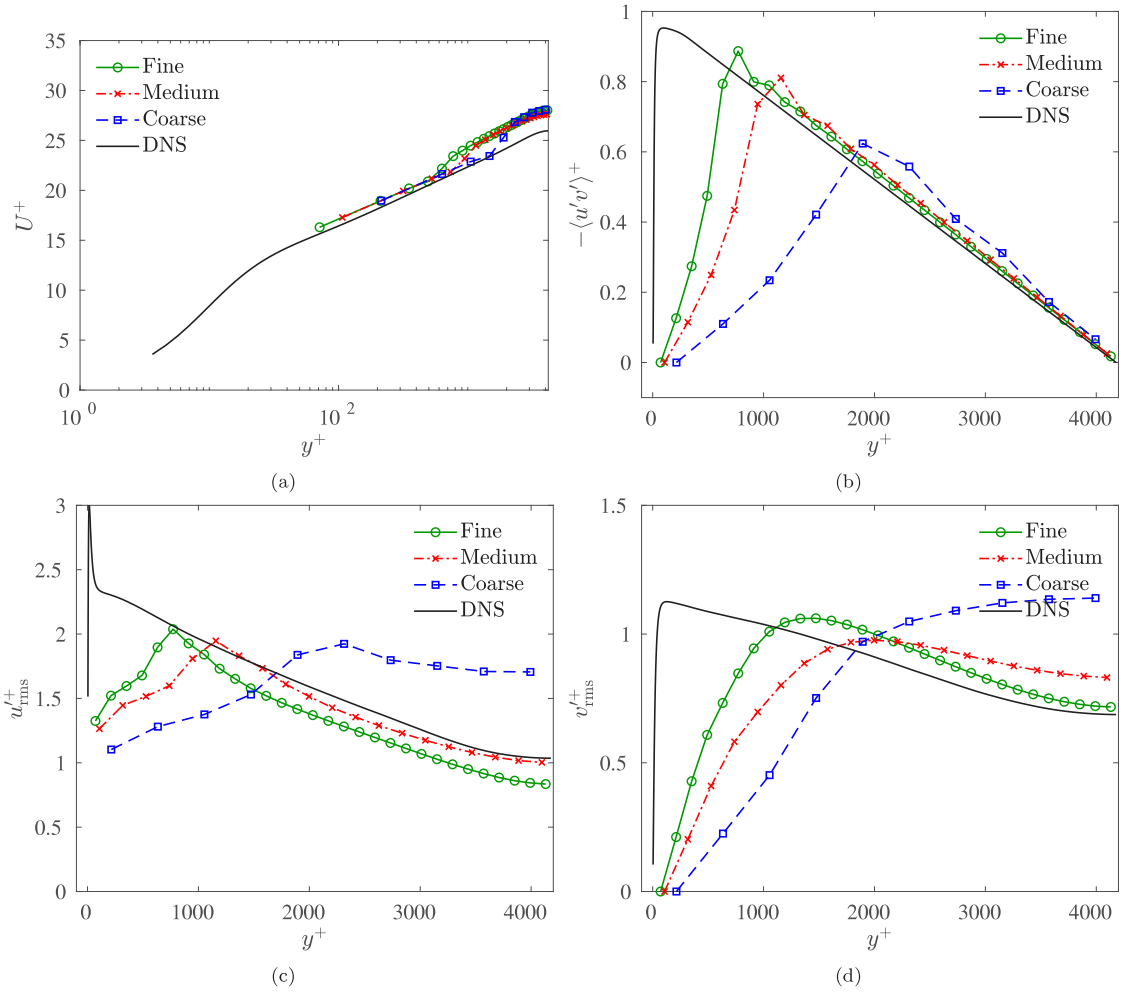

Fig. 7. Grid study of the turbulent channel flow at $Re_\tau = 4200$ using the simplified constrained model. (a) The mean streamwise velocity U; (b) the resolved Reynolds stress $-\langle u'v'\rangle^+ = -\langle u'v'\rangle/u_\tau^2$; (c) the rms of the streamwise velocity $u'^+_{\mathrm{rms}} = u'_{\mathrm{rms}}/u_\tau$; (d) the rms of the normal velocity $v'^+_{\mathrm{rms}} = v'_{\mathrm{rms}}/u_\tau$.

The blending coefficient here indicates the ratio of actually resolved turbulent production over the intended one. If the flow region has no LES content, $\beta = 0$ recovers to RANS. If the flow is fully resolved by LES, $\beta = 1$ gives the original LES formulation. Above blending model is slightly different from the dynamic hybrid RANS-LES model [50,51] in which the stress is blended instead of the eddy viscosity.

- Constrained model

Verma et al. [52] presented a Reynolds stress constrained SGS model, in which the constant in the eddy viscosity is adjusted dynamically to account for the deficits of the Reynolds stress

$$-2\nu_t^{\mathrm{RANS}}\langle\tilde{S}_{ij}\rangle = R_{ij}^{\mathrm{LES}} - 2C\Delta^2\langle|\tilde{S}^*|\tilde{S}_{ij}\rangle. \tag{43}$$

Using the least square method gives to

$$C\Delta^2 = \frac{2\nu_t^{\mathrm{RANS}}\langle\tilde{S}_{ij}\rangle\langle|\tilde{S}^*|\tilde{S}_{ij}\rangle + R_{ij}^{\mathrm{LES}}\langle|\tilde{S}^*|\tilde{S}_{ij}\rangle}{2\langle|\tilde{S}^*|\tilde{S}_{ij}\rangle\langle|\tilde{S}^*|\tilde{S}_{ij}\rangle}, \tag{44}$$

and consequently,

$$\nu_t^{\mathrm{hybrid}} = \frac{2\nu_t^{\mathrm{RANS}}\langle\tilde{S}_{ij}\rangle\langle|\tilde{S}^*|\tilde{S}_{ij}\rangle + R_{ij}^{\mathrm{LES}}\langle|\tilde{S}^*|\tilde{S}_{ij}\rangle}{2\langle|\tilde{S}^*|\tilde{S}_{ij}\rangle\langle|\tilde{S}^*|\tilde{S}_{ij}\rangle}|\tilde{S}^*|. \tag{45}$$

It should be noted that in [52] the dynamic Smagorinsky model is used along with the Reynolds stress constraint to determine the constant, similar to Chen et al. [53]. As mentioned previously, the dynamic procedure needs averaging in the homogeneous direction for stabilization and explicit filtering. Eq. (44) allows for more general LES eddy viscosity models with an appropriate choice of $|\tilde{S}^*|$, for example using $|\tilde{S}^*| = |\tilde{S}|$ for the classical Smagorinsky model. In [52] the constraint is controlled by a weight function which consists of an scaling factor for the constraint strength and a threshold value for the constraint region. In this work, the scaling factor is not considered for strict satisfaction of the Reynolds stress constraint (33) and the threshold is explicitly controlled via the wall distance.

- Simplified constrained model

By assuming that the hybrid eddy viscosity and the mean strain rate tensor are independent [49], the Reynolds stress balance equation (33) can be rewritten as

$$-2\nu_t^{\mathrm{RANS}}\langle\tilde{S}_{ij}\rangle = R_{ij}^{\mathrm{LES}} - 2\nu_t^{\mathrm{hybrid}}\langle\tilde{S}_{ij}\rangle, \tag{46}$$

therefore

$$\nu_t^{\mathrm{hybrid}} = \frac{2\nu_t^{\mathrm{RANS}}\langle\tilde{S}_{ij}\rangle\langle\tilde{S}_{ij}\rangle + R_{ij}^{\mathrm{LES}}\langle\tilde{S}_{ij}\rangle}{2\langle\tilde{S}_{ij}\rangle\langle\tilde{S}_{ij}\rangle}, \tag{47}$$

which can be viewed as a simplification to the constrained model but is functionally more closer to the dynamic model.

4.5. Summary of the near-wall treatment

The near-wall treatment of current immersed boundary based LES can be summarized as follows

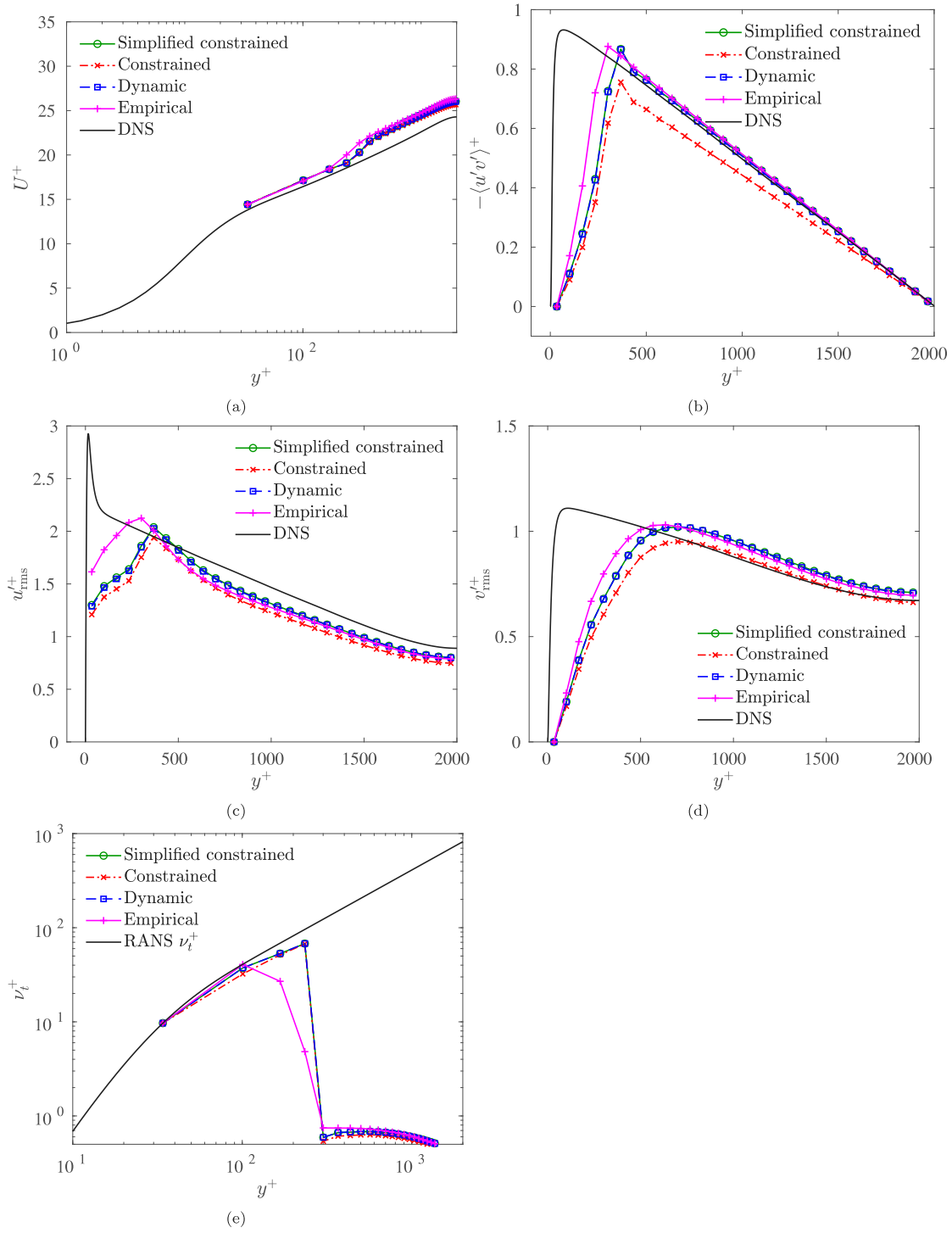

Fig. 8. Comparison of blending models for the turbulent channel flow at $Re_\tau = 2000$ on the fine grid. (a) The mean streamwise velocity U; (b) the resolved Reynolds stress $-\langle u'v'\rangle^+ = -\langle u'v'\rangle/u_\tau^2$; (c) the rms of the streamwise velocity $u'^+_{\mathrm{rms}} = u'_{\mathrm{rms}}/u_\tau$; (d) the rms of the normal velocity $v'^+_{\mathrm{rms}} = v'_{\mathrm{rms}}/u_\tau$; (e) the hybrid eddy viscosity $\nu_t^+ = \nu_t/\nu$.

1. Computing the tangential velocity and the friction velocity from the explicit wall model (25) at each donor cell around the boundary point;
2. Interpolating the friction velocity to the boundary point in wall-parallel plane using the IDW (26);
3. Calculating the boundary velocity from the explicit wall model (16) using the interpolated friction velocity;
4. Evaluating the velocity gradients with the WLSQ method and rectifying the wall-normal component from the wall model;
5. Imposing the RANS eddy viscosity at the boundary points and applying the eddy viscosity blending techniques in the near-wall grid points;
6. Reconstructing the particle distribution function in LBM from these macroscopic quantities at the surrogate boundary.

5. Numerical results

In order to assess the proposed near-wall treatments, we first consider the turbulent plane channel flow simulation in which the grids

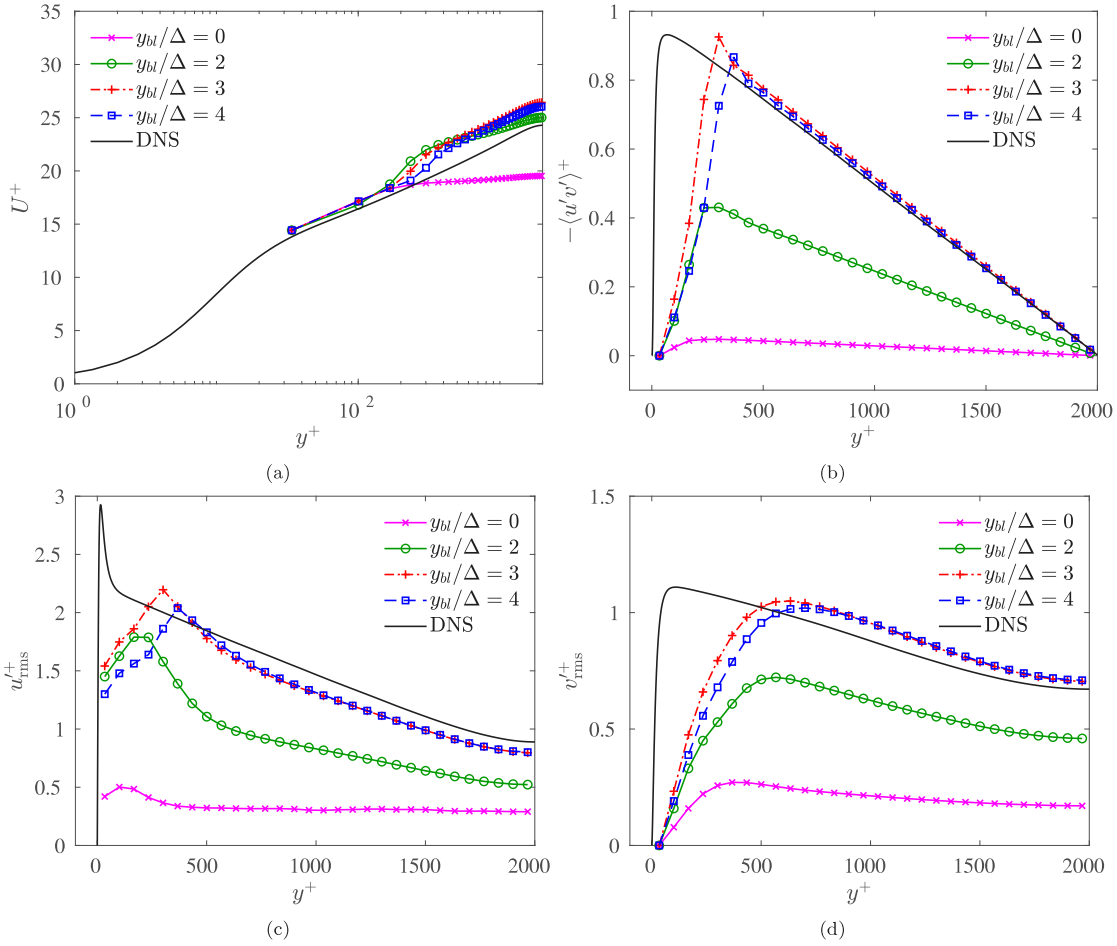

Fig. 9. Comparison of the blending region for the turbulent channel flow at $Re_\tau = 2000$ on the fine grid using the simplified constrained model. (a) The mean streamwise velocity U; (b) the resolved Reynolds stress $-\langle u'v'\rangle^+ = -\langle u'v'\rangle/u_\tau^2$; (c) the rms of the streamwise velocity $u'^+_{\rm rms} = u'_{\rm rms}/u_\tau$; (d) the rms of the normal velocity $v'^+_{\rm rms} = v'_{\rm rms}/u_\tau$.

are aligned to the wall plates. In this case the wall distance of the first off-wall grid points can be controlled, so that we can easily perform the sensitivity study of each model to the wall distance. Next we will consider a more general case with curved wall surfaces of complex shape, the turbulent flow over a three-element high-lift airfoil. The wall distance becomes arbitrary and no longer smooth along the wall, which allows us to demonstrate the capability of the proposed methods for obtaining smooth and accurate wall surface pressure and skin friction.

5.1. Turbulent channel flow

The turbulent plane channel flow is shown in Fig. 4, where the grids are parallel to the wall plates, in order to mimic the body-fitted situation. As a matter of fact, the fluid grids are seldom coincident with the wall surface in the context of IBM, hence the surrogate boundary is shifted away from the physical wall with a wall-normal distance denoted as y_b in current work (see Fig. 3), to study the sensitivity of the proposed methods with respect to the boundary wall distance. The computational domain is $2\pi\delta \times 2\delta \times 2\pi\delta$ covered by uniform grids ($\Delta x = \Delta y = \Delta z = \Delta$), with δ being the channel half width. Three grid resolutions are employed, namely the coarse grid, the medium grid and the fine grid, where the number of wall-normal grid points is $N = 10, 20, 30$ for the channel half width respectively. To address the finite Reynolds number effect, a series of Reynolds number $Re_\tau \equiv u_\tau\delta/\nu$ has been studied, ranging from 950 to 4200. It should be noted that the first off-wall grid point never resides in the viscous sublayer in all current simulations, hence the results are principally determined by the near-wall treatments.

Periodic boundary conditions are assumed in the streamwise and spanwise directions, while the near-wall treatments are applied in the wall-normal direction. In order to achieve the desired Reynolds number, an external body force is introduced and computed dynamically by

$$g = \frac{u_\tau^2}{\delta} + \frac{u_\tau - u_\tau^{\rm avg}}{\Delta t}, \tag{48}$$

where $u_\tau^{\rm avg}$ is the instantaneous friction velocity averaged over the surrogate boundary and $u_\tau = \nu Re_\tau/\delta$ is the target value.

The initial flow velocities are prescribed to the wall-law profile with random perturbations for facilitating rapid turbulence development. The perturbation strength is about 10% for the streamwise velocity and 5% for the other two components. After a transient state, the turbulent flow becomes fully established, then the statistics are collected over a sufficient long time period.

5.1.1. Reynolds number dependency

The mean streamwise velocity and the resolved Reynolds stresses are shown in Figs. 5–7 for the turbulent channel flow using the simplified constrained model on different grids, at the Reynolds number $Re_\tau = 950$, 2000 and 4200 respectively. The Smagorinsky constant $C_s = 0.1$ is used in the Vreman subgrid model. The surrogate boundary is lifted from the wall plate by 0.5Δ. The blending distance y_{bl} is fixed to 4Δ. As the normal velocity is set to zero at the boundary points, no Reynolds stress is resolved at the first off-wall grid points and the blending takes effect at the second, third and forth off-wall grid points. It should be noticed that the turbulent fluctuations are still resolved

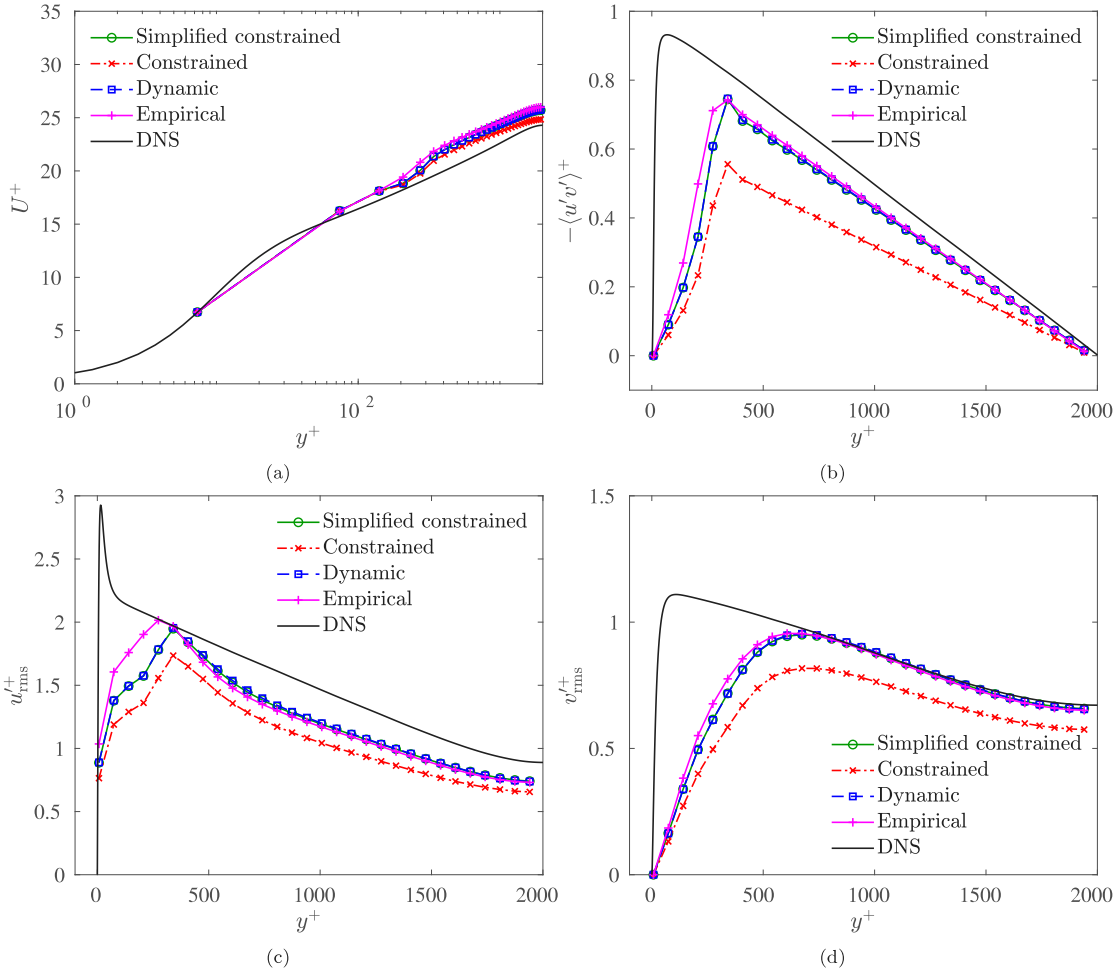

Fig. 10. Turbulent channel flow at $Re_\tau = 2000$ on the fine grid, with a boundary wall shift of $y_b = 0.1\Delta$. (a) The mean streamwise velocity U; (b) the resolved Reynolds stress $-\langle u'v'\rangle^+ = -\langle u'v'\rangle/u_\tau^2$; (c) the rms of the streamwise velocity $u'^+_{\mathrm{rms}} = u'_{\mathrm{rms}}/u_\tau$; (d) the rms of the normal velocity $v'^+_{\mathrm{rms}} = v'_{\mathrm{rms}}/u_\tau$.

inside the blending area, regardless the augmentation of subgrid eddy viscosity. It was demonstrated in [52,53] that the blending would not dissipate away the smaller scales of turbulence.

The mean streamwise velocity U on the near-wall grid points that are impacted by the eddy viscosity blending follows well the DNS data of [55]. Whereas it shows a small shift-up in the pure LES region in the inertial layer, known as the log-layer mismatch, which has been frequently observed in many hybrid RANS-LES methods [56,57]. The velocity jump occurs near the blending height, which corresponds to the jump of the Reynolds stress. It was revealed in [52,53] that the constrained subgrid models could eliminate the log-layer mismatch effectively on traditional body-fitted grid where the wall-normal grid is refined to resolve the steep velocity gradient, but the wall-parallel grid spacing is relatively larger than the boundary-layer thickness. Verma et al. [52] further relaxed the wall-normal grid resolution and found that the constrained model, when worked as a wall model, failed to remove the log-layer mismatch as well.

The resolved Reynolds stress $\langle u'v'\rangle^+$ outside the blending region converges well to the DNS results under grid refinement. It can be seen that on the coarse grid, the rms of both the streamwise and normal velocities deviate considerably from the DNS data with increasing Reynolds number, implying that a significant portion of turbulent structures is not well resolved. On the fine grid, the rms of the streamwise velocity u'^+_{rms} at $Re_\tau = 950$ agrees well with the DNS results, but becomes under-predicted as the Reynolds number increases. This is because the grid resolution in wall units Δ^+ gets coarsen for higher Reynolds number. Meanwhile the rms of the normal velocity v'^+_{rms} is slightly over-predicted away from the wall, which however moves closer to the DNS result as the Reynolds number increases. The correct boundary condition for the normal velocity can be tricky in the context of IBM. The zero normal velocity approximation made in this work provides rather good predictions anyway. One can also observe that the resolved Reynolds stresses $\langle u'v'\rangle^+$ and u'^+_{rms} exhibit a sharp transition right after the blending height, which is due to the sudden reduction of the eddy viscosity.

5.1.2. *Effect of blending models*

Fig. 8 compares different eddy viscosity blending models at $Re_\tau = 2000$ on the fine grid. The wall distance of the surrogate boundary and the blending height are kept to 0.5Δ and 4Δ respectively. For the empirical blending method, $\alpha = 0.4$ and $\gamma = 2$ are used, as recommended in [15]. Therefore, the blending starts from 1.6Δ, namely the third off-wall grid points, as opposed to the second point in the other models.

The mean streamwise velocity is predicted very closely among all the blending models but the log-layer mismatch issue persists. The peak values of the Reynolds stresses are slightly higher in the empirical blending model and the transition is relatively smooth across the blending height, despite that the empirical blending model does not strictly satisfies the Reynolds stress balance. This can be explained by the hybrid eddy viscosity in the blending region which is reduced gradually in the empirical blending model.

The constrained model produces a relatively smaller Reynolds stresses, consequently the rms of the normal velocity v'^+_{rms} matches well the DNS results. It can be seen that the profiles almost collapse between

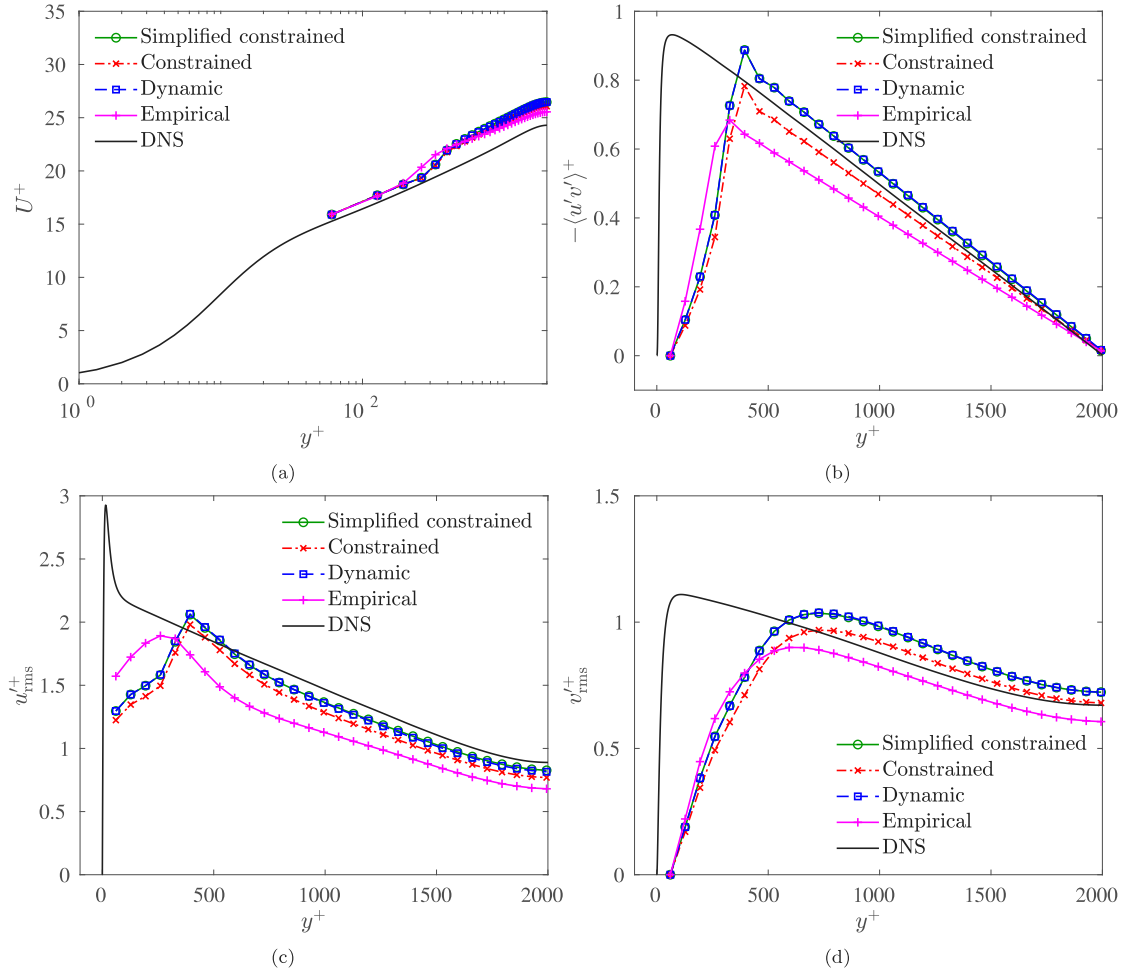

Fig. 11. Turbulent channel flow at $Re_\tau = 2000$ on the fine grid, with a boundary wall shift of $y_b = 0.9\Delta$. (a) The mean streamwise velocity U; (b) the resolved Reynolds stress $-\langle u'v'\rangle^+ = -\langle u'v'\rangle/u_\tau^2$; (c) the rms of the streamwise velocity $u'^+_{\mathrm{rms}} = u'_{\mathrm{rms}}/u_\tau$; (d) the rms of the normal velocity $v'^+_{\mathrm{rms}} = v'_{\mathrm{rms}}/u_\tau$.

the simplified constrained model and the dynamic model. This may come from the use of the time-averaged strain rate tensor $\langle \tilde{S}_{ij} \rangle$ for the tensor product in their least square minimization.

Enforcing the Reynolds stress balance in present work principally aims at overcoming the stress loss. This can be verified from Fig. 9 for different blending height in the simplified constrained model at $Re_\tau = 2000$ on the fine grid. A significant amount of stress loss is observed when reducing the eddy viscosity blending region towards zero, which was also observed in [15]. To maintain the total Reynolds stress, the blending should be applied to at least the second and the third off-wall grid points, or equivalently $y_{bl} = 3\Delta$ in this case.

5.1.3. Influence of boundary wall distance

The wall distance of the surrogate boundary demonstrates a very strong impact. Figs. 8, 10 and 11 compare all blending models at $Re_\tau = 2000$ on the fine grid for different boundary wall distances of $y_b = 0.5\Delta$, 0.1Δ and 0.9Δ respectively. The blending height is $y_{bl} = 4\Delta$ for all the blending models.

The non-dimensional mean streamwise velocity is not very sensitive to the boundary wall distance. On the contrary, the resolved Reynolds stresses are significantly changed with different boundary wall distances. As the surrogate boundary moves close to the wall, the level of resolved stresses gets decreased for all blending models, especially for the constrained model in which the stresses are strongly under-predicted. Lifting up from the wall, the constrained model is improved for the resolved stresses whereas the empirical model leads to considerable under-predictions. That could be explained by the fact that the empirical model does not fulfill the Reynolds stress balance, hence it shows a stronger dependency on the boundary wall distance.

5.2. 30P30N three-element airfoil

Now we consider a more complex benchmark test case that is relevant to industrial applications, the modified-slat 30P30N three-element high-lift airfoil where the deflection angles of the slat and the flap are both 30°. This case has been extensively studied for aerodynamics and acoustics, for which various experimental and numerical results are available for comparison [58–60]. The Mach number is 0.17 and the Reynolds number is 1.71×10^6 based on the free-stream velocity U_∞ and the stowed chord c. The angle of attack of 5.5° is considered by inclining the incoming flow.

The computational domain is chosen to $[90c, 60c, 0.14c]$ in present study. The flow travels over a distance of $30c$ from the inlet to the airfoil and exits the domain after $60c$. The lateral boundaries are maintained $30c$ away from the airfoil. Absorbing layers are applied in the vicinity of outer boundaries to reduce spurious reflection of the flow back into the domain. The entire simulation is carried out for 28 flow-through times (c/U_∞) and the time-averaging is performed over the last 14 flow-though times such that the turbulence statistics are converged.

Two grids are employed to check the sensitivity of the proposed treatments to the near-wall grid resolution. The grid spacing far away from the airfoil is around $0.14c$ for both grids that is progressively refined towards the airfoil using the Octree architecture. The near-wall grid spacing of the coarse grid is around $1.1 \times 10^{-3}c$ and the number

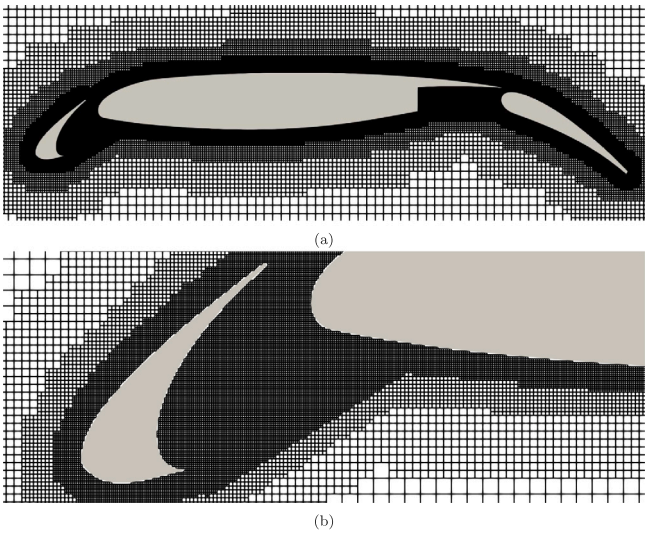

Fig. 12. Computational grid for the 30P30N high-lift three-element airfoil. (a) the overall grid around the airfoil; (b) the slat region.

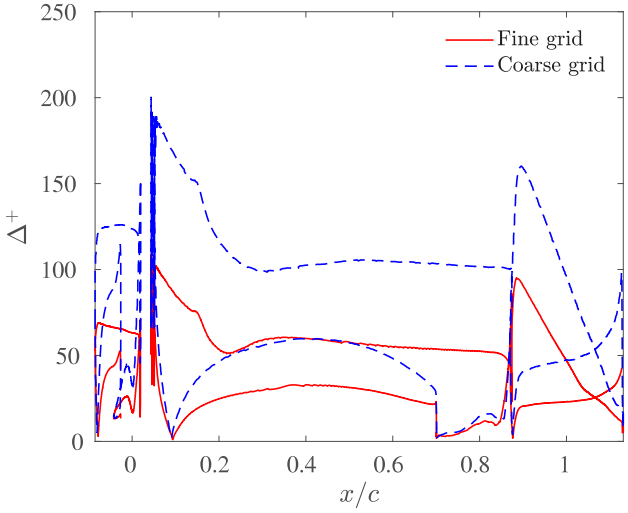

Fig. 13. Near-wall grid resolution for the 30P30N high-lift three-element airfoil.

of total grid points is about 8 million. An additional near-wall grid refinement is taken in the fine grid which leads to the near-wall grid spacing about $5.5 \times 10^{-4}c$ and the total grid points of approximate 55 million. Figs. 12 and 13 display the grid distribution near the airfoil and the grid resolution respectively. Generally speaking the near-wall grid resolution should be further refined especially near the leading edge of the main element, but current grids give rather good predictions of the overall aerodynamic quantities. Table 1 shows the coefficients of drag and lift integrated on the surrogate boundaries using the far-field approach [16]. These integral quantities with all blending models are close to available experimental and numerical results, indicating the accuracy and efficiency of current near-wall modeling.

The mean wall pressure $C_p = (p_w - p_\infty)/(1/2\rho_\infty U_\infty^2)$ and the mean skin friction $C_f = \rho u_\tau^2/(1/2\rho_\infty U_\infty^2)$ are shown in Figs. 14 and 15 for different treatments of the eddy viscosity on the coarse grid and the fine grid respectively, where p_∞ and ρ_∞ represent the free-stream pressure and density. The blending height is fixed to 4Δ for all the eddy viscosity blending models. The overall profiles are smooth, except near the leading edge of the main element where the turbulent boundary layer is too thin for current grid resolution. Therefore, it can be said that the wall ingredients (interpolation for u_τ, WLSQ gradient scheme and wall-law normal gradient) in RANS for smoothing wall surface quantities works equivalently well in current LES near-wall treatment.

The mean wall pressure on the lower surface agrees well with the experimental data of Murayama et al. [58] and Pascioni et al. [59]. On the upper surface of the main element, the predicted mean wall pressure lies between the two data sets on the coarse grid. Nevertheless noticeable deviation is found towards the upper surface of the flap and slat elements from both experiments, which can be attributed to the coarse grid resolution. It can be seen that the mean wall pressure well converges to the experimental results of Murayama et al. [58] on the fine grid. On the other side, the wall pressure shows negligible variations with respect to different hybrid eddy viscosity models.

However the mean skin friction is affected by different treatments of the eddy viscosity. The result obtained with the empirical model differs from the others on the upper surfaces where the turbulence is developing. Enforcing the exact Reynolds stress balance near-wall gives almost indistinguishable mean skin friction among the constrained, dynamic and simplified constrained models. It is also noticed that the predicted mean skin friction is increased on the upper surface as the grid is refined. This quantity is rarely presented in the literature and large discrepancies are observed in its values even with Navier–Stokes based body fitted methods. We present it here for future reference.

Fig. 16 displays the sensitivity of blending height in different eddy viscosity blending models on the coarse grid. It is observed that the empirical model is more sensitive to blending region. When reducing the blending height, the mean skin friction is increased significantly over the entire upper surfaces in the empirical model and the wall pressure difference becomes visible as well. Models that fulfill the Reynolds stress constraint are more robust. Although the laminar-turbulent transition location is still sensitive to the blending height, but the remaining parts are essentially not changed for the constrained, dynamic and simplified constrained models. In the following results, we focus on the blending height $y_{bl} = 4\Delta$.

The flow inside the slat cove contains a lot of physical phenomena that are very important to the aerodynamic performance. The shear layer coming from the lower cusp rolls up into spanwise vortices, which can be visualized from the isosurfaces of the Q-criterion in Fig. 17 and the instantaneous spanwise vorticity in Fig. 18. The coherent structures impinge on the lower slat surface and create a recirculation zone between the slat and main element. The mean streamline is shown in Fig. 18(c) that clearly reveals the flow recirculation inside the

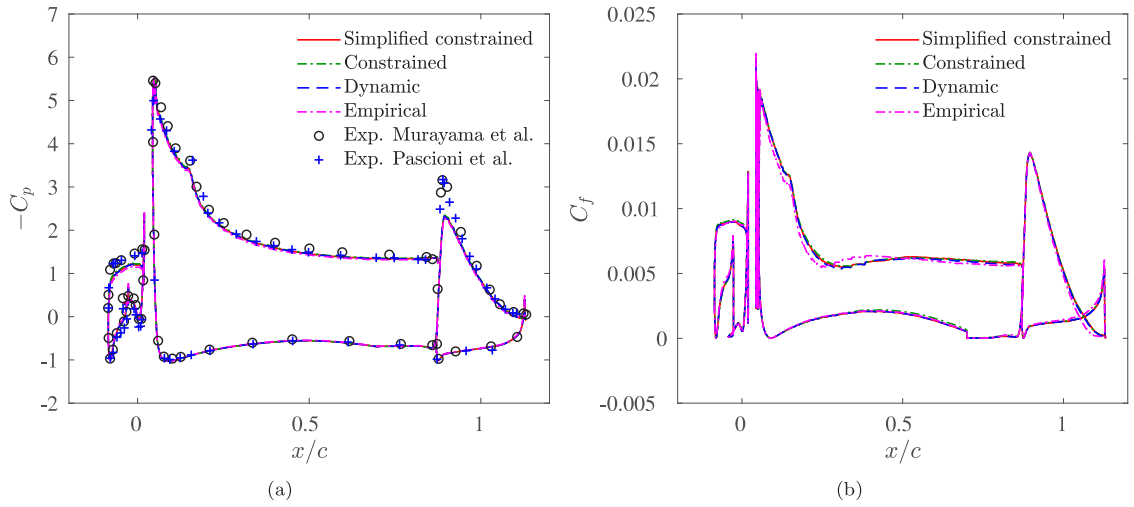

Fig. 14. Comparison of blending models for the mean wall surface pressure $C_p = (p_w - p_\infty)/(1/2\rho_\infty U_\infty^2)$ and the mean skin friction $C_f = \rho u_\tau^2/(1/2\rho_\infty U_\infty^2)$ for the 30P30N high-lift three-element airfoil, on the coarse grid. The Experimental results are digitized from Murayama et al. [58] (circle) and Pascioni et al. [62] (plus) respectively.

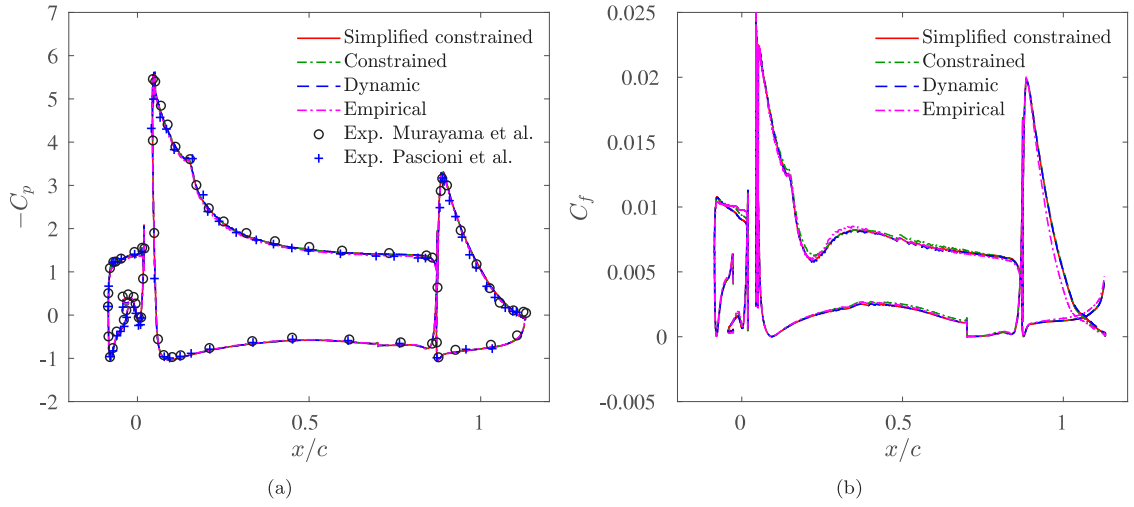

Fig. 15. Comparison of blending models for the mean wall surface pressure $C_p = (p_w - p_\infty)/(1/2\rho_\infty U_\infty^2)$ and the mean skin friction $C_f = \rho u_\tau^2/(1/2\rho_\infty U_\infty^2)$ for the 30P30N high-lift three-element airfoil, on the fine grid. The Experimental results are digitized from Murayama et al. [58] (circle) and Pascioni et al. [62] (plus) respectively.

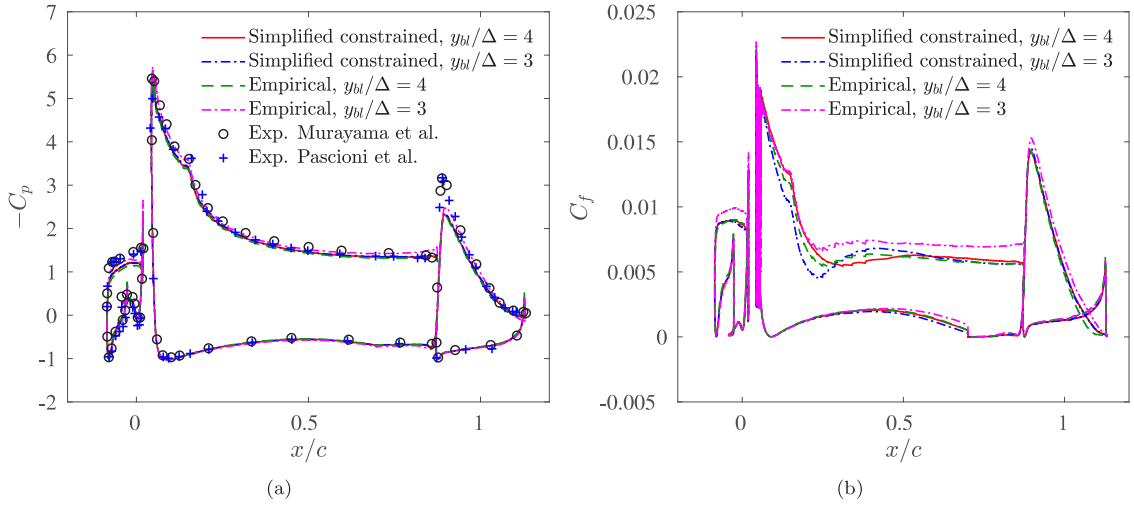

Fig. 16. Comparison of blending heights for the mean wall surface pressure $C_p = (p_w - p_\infty)/(1/2\rho_\infty U_\infty^2)$ and the mean skin friction $C_f = \rho u_\tau^2/(1/2\rho_\infty U_\infty^2)$ for the 30P30N high-lift three-element airfoil, on the coarse grid. The Experimental results are digitized from Murayama et al. [58] (circle) and Pascioni et al. [62] (plus) respectively.

Table 1
Comparison of blending models for the drag and lift coefficients for the 30P30N high-lift airfoil, where N/A denotes "not available".

	Method	C_d		C_l	
		Coarse	Fine	Coarse	Fine
Murayama et al. [58]	Experiment	N/A		≈2.8	
Choudhari et al. [61]	Experiment	N/A		≈2.6	
Pascioni et al. [62]	Experiment	N/A		≈2.8	
Ashton et al. [60]	IDDES, structured grid	0.135		2.631	
	IDDES, unstructured grid	0.184		2.648	
Zhang et al. [63]	WMLES, structured grid	0.06926	0.06740	2.852	2.848
Present	Simplified constrained blending	0.110	0.078	2.628	2.827
	Constrained blending	0.107	0.076	2.647	2.824
	Dynamic blending	0.109	0.078	2.621	2.829
	Empirical blending	0.113	0.078	2.573	2.775

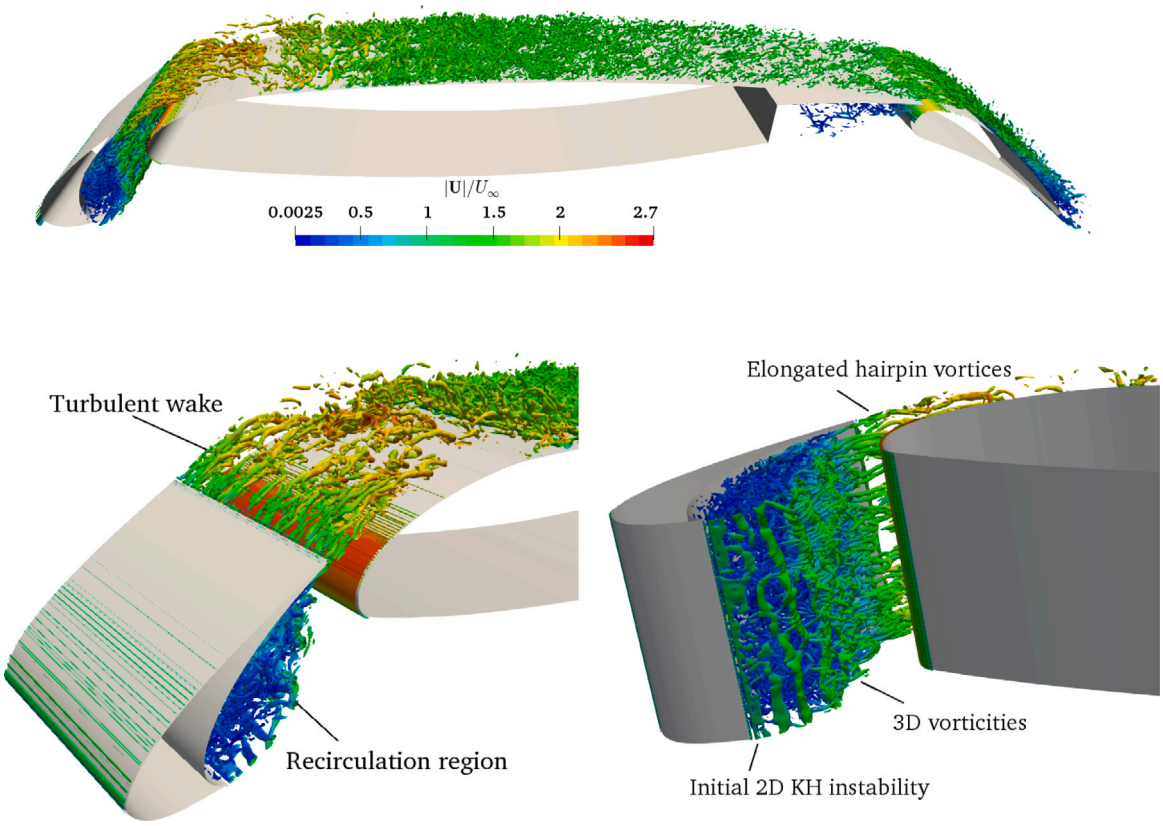

Fig. 17. Isosurfaces of the Q-criterion ($Qc^2/U_\infty^2 = 6257$) using the simplified constrained model on the fine grid, colored by the velocity magnitude.

slat cove. Good agreements are found between these results with the stereoscopic particle image velocimetry results of Pascioni et al. [59]. Further details can be examined on the flow velocity along the sampled lines defined in Fig. 19. All the blending models show a good trend far away from the lower slat surface and match well with the experiments. The deviation becomes evident when approaching the slat wall. The dynamic model and the simplified constrained model give very accurate prediction of the velocity behavior, followed by the constrained model. The empirical model that gives considerable over-estimation of the flow velocity is the least accurate. This highlights the importance of the Reynolds stress balance in the near-wall region.

To further demonstrate the capability of the proposed method, a more challenging case, namely the MDA 30P/30N at the maximum lift configuration, is simulated at the angle of attack of 21° with the simplified constrained model. The Reynolds number is 5×10^6 and the Mach number is 0.2. The results are compared to the well established experimental data [64]. In order to reduce the computational cost, the spanwise length is reduced to $0.07c$. The finest grid spacing around the airfoil is about $5.5 \times 10^{-4}c$ and the total grid number is around 29 million.

Fig. 20 shows the mean wall pressure and the mean skin friction. Even though some discrepancies can be observed against the experiments, the overall prediction is fairly good, considering the fact that the grid resolution at this Reynolds number is actually coarse ($\Delta^+ = 3.2$~340). There are certainly rooms for further grid refinement, however the main contribution of this work is to reduce the grid requirement as much as possible while retaining a good level of accuracy for complex turbulent flow simulations. The key achievement of the proposed method is to ensure the Reynolds stress balance near wall and the physical prediction of the wall surface quantities on immersed grids under coarse resolution. It should also be highlighted that the hybrid viscosity in dynamic modes is able to return to the subgrid eddy

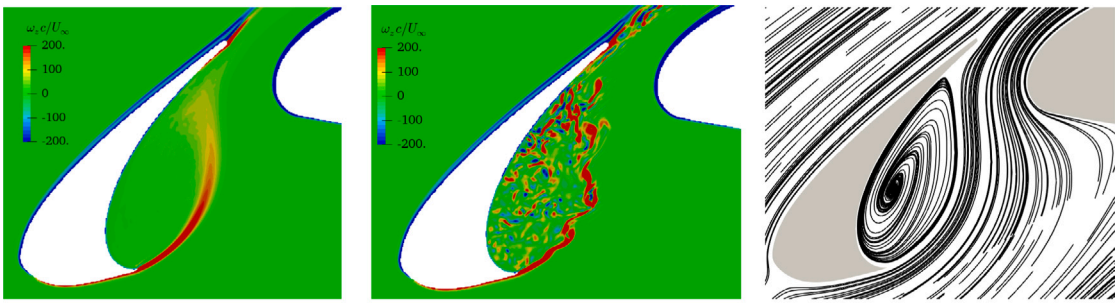

Fig. 18. Flow fields near the slat region using the simplified constrained model on the fine grid. (a) Mean vorticity $\omega_z c/U_\infty$; (b) instantaneous vorticity; (c) mean streamline.

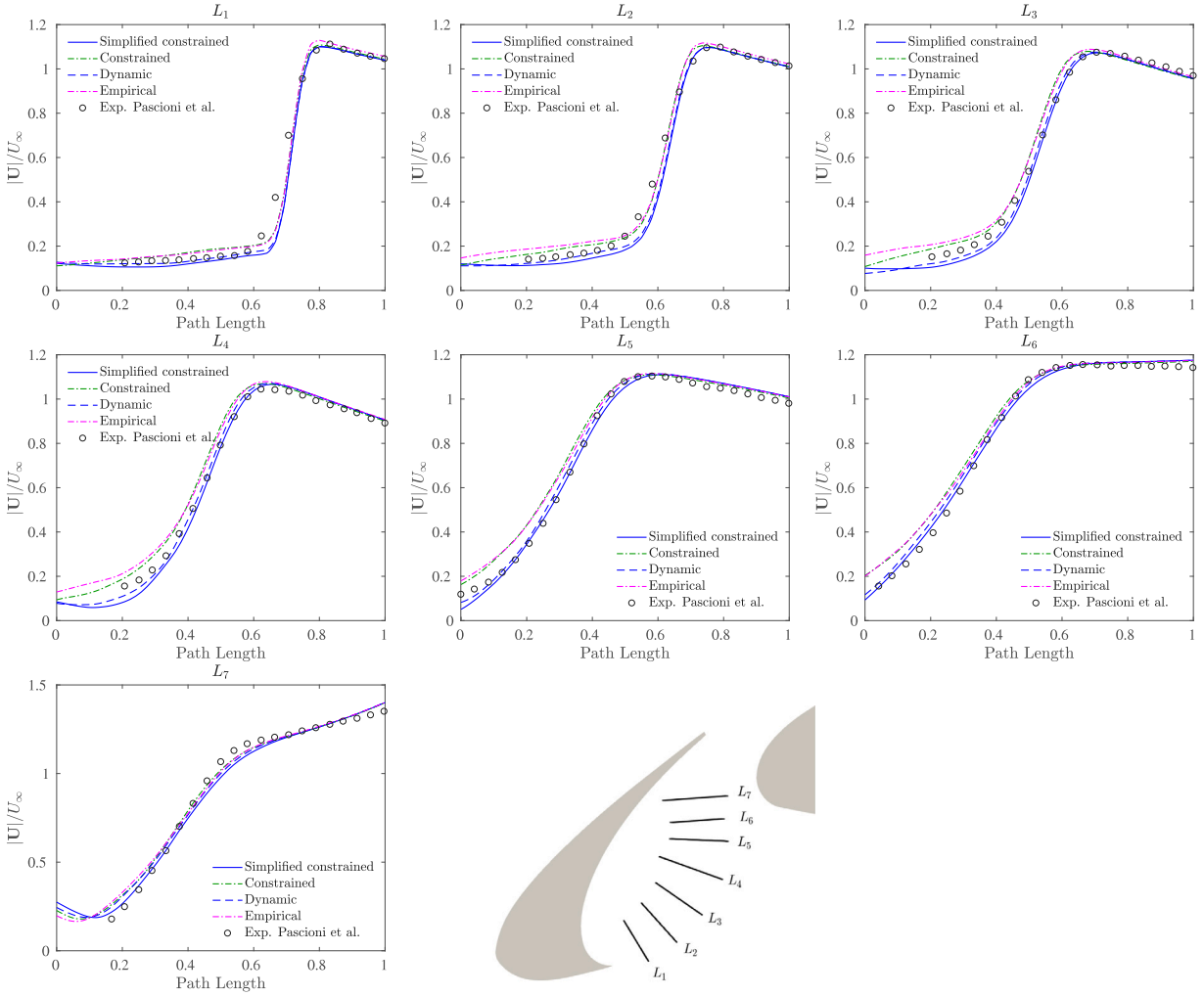

Fig. 19. Comparison of blending models for the mean velocity profiles over sample lines near the slat region on the fine grid. The Experimental results are digitized from Pascioni et al. [59] (circles).

viscosity near wall, namely the wall-modeled large eddy simulation, in case of highly refined grids or flow separations. This could be very advantageous for more complex industrial flow simulations.

6. Conclusions

In this work a coupled IBM-LES near-wall modeling for high Reynolds number turbulent flows over complex geometries on Cartesian grids has been presented. It is based on an extension of the previously developed near-wall ingredients from RANS to LES mode. Furthermore the hybrid RANS-LES strategy is applied to the near-wall eddy viscosity and various formulations have been investigated. The empirical blending method is simple to use and effective, but the results are sensitive to the wall distance of the surrogate boundary and the blending height. Enforcing the Reynolds stress constraint exactly turns out to be more robust even if it requires dynamic extraction of the mean quantities. The choice of the weight for minimizing the Reynolds stress constraint is of paramount importance, and it has been found that using the mean strain rate gives the best results. Based on that, a novel hybrid eddy viscosity model is proposed. Additionally, an

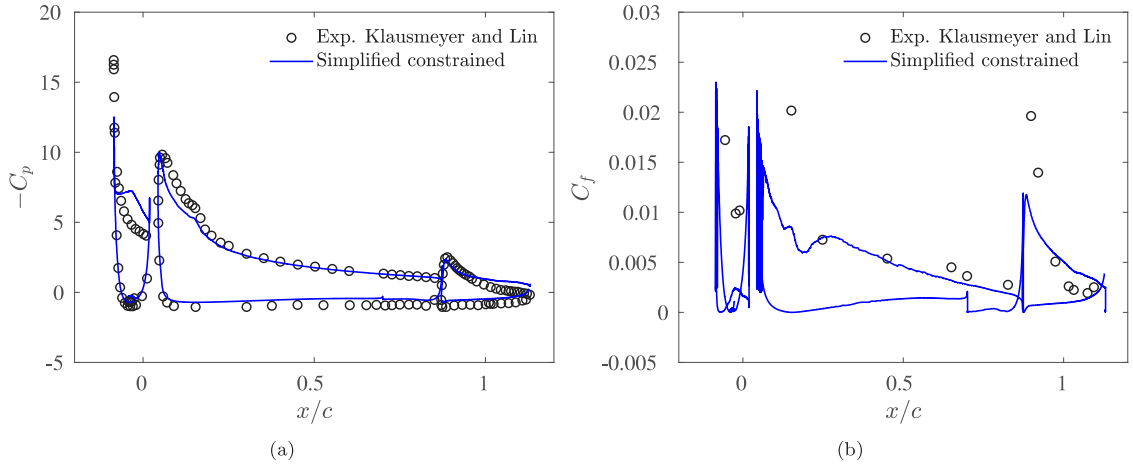

Fig. 20. The mean wall surface pressure $C_p = (p_w - p_\infty)/(1/2\rho_\infty U_\infty^2)$ and the mean skin friction $C_f = \rho u_\tau^2/(1/2\rho_\infty U_\infty^2)$ for the MDA 30P30N maximum lift configuration. The Experimental results are digitized from Klausmeyer and Lin [64] (circle).

adapted explicit wall model covering the viscous sublayer, the buffer layer and the logarithmic layer is introduced to reduce the unnecessary computational cost as much as possible.

This new near-wall modeling has been assessed by considering first the well-known turbulent channel flow configuration and then a complex three-element high-lift airfoil geometry. Very satisfactory results were obtained in terms of the mean velocity and the Reynolds stress profiles in comparison with the DNS data for the turbulent channel flow configuration. The results obtained on the 30P30N airfoil indicate that the RANS wall ingredients have been successfully extended to LES to obtain smooth time-averaged wall pressure and skin friction coefficients on complex curved wall surfaces, even at a significantly higher angle of attack of 21° for the maximum lift configuration. Moreover, the integral drag and lift coefficients, the flow structures and the velocity profiles are all well predicted with the proposed method, highlighting the suitability for industrial applications. Even though the lattice Boltzmann method has been used in this work, the current near-wall treatment is versatile as it can be applied to the Navier–Stokes based solvers straightforwardly. More complex industrial applications, possibly including massive flow separations, will be considered in the future work.

CRediT authorship contribution statement

Shang-Gui Cai: Conceptualization, Methodology, Software, Validation, Formal analysis, Writing – original draft. **Jérôme Jacob:** Software, Ressources, Writing – review & editing, Supervision. **Pierre Sagaut:** Project administration, Supervision, Resources, Writing – review & editing.

Declaration of competing interest

The authors declare that they have no known competing financial interests or personal relationships that could have appeared to influence the work reported in this paper.

Data availability

Data will be made available on request.

Acknowledgments

This work was carried out with the ProLB solver. Centre de Calcul Intensif d'Aix-Marseille is acknowledged for granting access to its high performance computing resources. This work was performed using HPC resources from GENCI-TGCC (Grant 2021-A0092A07679). We acknowledge the supports of the DGAC project No 2018-16 OMEGA3 and the ANR Industrial Chair ALBUMS (grant ANR-18-CHIN-0003-01). Dr. Kyle A. Pascioni is acknowledged for providing the experimental data for the 30P30N multi-element airfoil.

References

[1] Peskin CS. Flow patterns around heart valves: A numerical method. J Comput Phys 1972;10(2):252–71.
[2] Iaccarino G, Verzicco R. Immersed boundary technique for turbulent flow simulations. Appl Mech Rev 2003;56(3):331–47.
[3] Mittal R, Iaccarino G. Immersed boundary method. Annu Rev Fluid Mech 2005;37(1):239–61.
[4] Sotiropoulos F, Yang X. Immersed boundary methods for simulating fluid-structure interaction. Prog Aerosp Sci 2014;65:1–21.
[5] Griffith BE, Patankar NA. Immersed methods for fluid–structure interaction. Annu Rev Fluid Mech 2020;52:421–48.
[6] Fadlun E, Verzicco R, Orlandi P, Mohd-Yusof J. Combined immersed-boundary finite-difference methods for three-dimensional complex flow simulations. J Comput Phys 2000;161(1):35–60.
[7] Tseng Y-H, Ferziger J. A ghost-cell immersed boundary method for flow in complex geometry. J Comput Phys 2003;192:593–623.
[8] Mittal R, Dong H, Bozkurttas M, Najjar F, Vargas A, von Loebbecke A. A versatile sharp interface immersed boundary method for incompressible flows with complex boundaries. J Comput Phys 2008;227(10):4825–52.
[9] Uhlmann M. An immersed boundary method with direct forcing for the simulation of particulate flows. J Comput Phys 2005;209(2):448–76.
[10] Taira K, Colonius T. The immersed boundary method: A projection approach. J Comput Phys 2007;225(2):2118–37.
[11] Cai S-G, Ouahsine A, Favier J, Hoarau Y. Moving immersed boundary method. Internat J Numer Methods Fluids 2017;85:288–323.
[12] Capizzano F. Turbulent wall model for immersed boundary methods. AIAA J 2011.
[13] Tamaki Y, Harada M, Imamura T. Near-wall modification of Spalart–Allmaras turbulence model for immersed boundary method. AIAA J 2017.
[14] Wilhelm S, Jacob J, Sagaut P. An explicit power-law-based wall model for lattice Boltzmann method-Reynolds-averaged numerical simulations of the flow around airfoils. Phys Fluids 2018;30.
[15] Maeyama H, Imamura T, Osaka J, Kurimoto N. Turbulent channel flow simulations using the lattice Boltzmann method with near-wall modeling on a non-body-fitted Cartesian grid. Comput Math Appl 2021;93:20–31.
[16] Cai S-G, Degrigny J, Boussuge J-F, Sagaut P. Coupling of turbulence wall models and immersed boundaries on Cartesian grids. J Comput Phys 2021;429:109995.
[17] Knopp T, Alrutz T, Schwamborn D. A grid and flow adaptive wall-function method for RANS turbulence modelling. J Comput Phys 2006;220(1):19–40.
[18] Degrigny J, Cai S-G, Boussuge J-F, Sagaut P. Improved wall model treatment for aerodynamic flows in LBM. Comput & Fluids 2021;105041.

[19] Constant B, Péron S, Beaugendre H, Benoit C. An improved immersed boundary method for turbulent flow simulations on Cartesian grids. J Comput Phys 2021;435:110240.
[20] Xu Y, Liu X. An immersed boundary method with y^+-adaptive wall function for smooth wall shear. Internat J Numer Methods Fluids 2021;93(6):1929–46.
[21] Tessicini F, Iaccarino G, Fatica M, Wang M, Verzicco R. Wall modeling for large-eddy simulation using an immersed boundary method. In: Annu. res. briefs. Cent. Turbul. Res.; 2002, p. 181–7.
[22] Cristallo A, Verzicco R. Combined immersed boundary/large-eddy-simulations of incompressible three dimensional complex flows. Flow Turbul Combust 2006;77:3–26.
[23] Balaras E, Benocci C, Piomelli U. Two-layer approximate boundary conditions for large-eddy simulation. AIAA J 1996;34(6):1111–9.
[24] Chester S, Meneveau C, Parlange MB. Modeling turbulent flow over fractal trees with renormalized numerical simulation. J Comput Phys 2007;225:427–48.
[25] Roman F, Armenio V, Frohlich J. A simple wall-layer model for large eddy simulation with immersed boundary method. Phys Fluids 2009;21:101701.
[26] Kang S. An improved near-wall modeling for large-eddy simulation using immersed boundary methods. Internat J Numer Methods Fluids 2015;78(2):76–88.
[27] Jiménez J, Vasco C. Approximate lateral boundary conditions for turbulent simulations. In: Annu. res. briefs. Cent. Turbul. Res.; 1998, p. 399–412.
[28] Chung D, Pullin DI. Large-eddy simulation and wall modelling of turbulent channel flow. J Fluid Mech 2009;631:281–309.
[29] Inoue M, Pullin D. Large-eddy simulation of the zero-pressure-gradient turbulent boundary layer up to $Re_\theta = O(10^{12})$. J Fluid Mech 2011;686:507–33.
[30] Cheng W, Pullin D, Samtaney R. Large-eddy simulation of separation and reattachment of a flat plate turbulent boundary layer. J Fluid Mech 2015;785:78–108.
[31] Gao W, Zhang W, Cheng W, Samtaney R. Wall-modelled large-eddy simulation of turbulent flow past airfoil. J Fluid Mech 2019;873:174–210.
[32] Wang H-N, Huang W-X, Xu C-X. Off-wall boundary conditions for large-eddy simulation based on near-wall turbulence prediction. Phys Fluids 2021;33:045125.
[33] Bose S, Park G. Wall-modeled large-eddy simulation for complex turbulent flows. Annu Rev Fluid Mech 2018;50:535–61.
[34] Bose S, Moin P. A dynamic slip boundary condition for wall-modeled large-eddy simulation. Phys Fluids 2014;2014:015104.
[35] Bae H, Lozano-Duràn A, Bose S, Moin P. Dynamic slip wall model for large-eddy simulation. J Fluid Mech 2019;859:400–32.
[36] Germano M, Piomelli U, Moin P, Cabot W. A dynamic subgrid-scale eddy viscosity model. Phys Fluids A 1991;3(7):1760–5.
[37] Lilly DK. A proposed modification of the Germano subgrid-scale closure method. Phys Fluids A 1992;4(3):633–5.
[38] Vreman A. An eddy-viscosity subgrid-scale model for turbulent shear flow: Algebraic theory and applications. Phys Fluids 2004;16(10):1070–6631.
[39] Jacob J, Malaspinas O, Sagaut P. A new hybrid recursive regularised Bhatnagar-Gross-Krook collision model for Lattice Boltzmann method-based large eddy simulation. J Turbul 2018;19:1–26.
[40] Cai S-G, Sagaut P. Explicit wall models for large eddy simulation. Phys Fluids 2021;33(4):041703.
[41] Latt J, Chopard B. Straight velocity boundaries in the lattice Boltzmann method. Phys Rev E 2008;77:056703.
[42] Kawai S, Larsson J. Wall-modeling in large eddy simulation: Length scales, grid resolution, and accuracy. Phys Fluids 2012;24:015105.
[43] Fakhari A. A new wall model for large eddy simulation of separated flows. Fluids 2019;4:197.
[44] Cabot W, Moin P. Approximate wall boundary conditions in the large-eddy simulation of high Reynolds number flow. Flow Turbul Combust 2000;63:269–91.
[45] Wang M, Moin P. Dynamic wall modeling for large-eddy simulation of complex turbulent flows. Phys Fluids 2002;14(7):2043–51.
[46] Kawai S, Larsson J. A dynamic wall model for large-eddy simulation of high Reynolds number compressible flows. In: Annu. res. briefs. Cent. Turbul. Res.; 2010, p. 25–37.
[47] Kawai S, Larsson J. Dynamic non-equilibrium wall-modeling for large eddy simulation at high Reynolds numbers. Phys Fluids 2013;25:015105.
[48] Park G, Moin P. An improved dynamic non-equilibrium wall-model for large eddy simulation. Phys Fluids 2014;26:015108.
[49] Templeton J, Medic G, Kalitzin G. An eddy-viscosity based near-wall treatment for coarse grid large-eddy simulation. Phys Fluids 2005;17:015101.
[50] Bhushan S, Walters D. A dynamic hybrid Reynolds-averaged Navier-Stokes-large eddy simulation modeling framework. Phys Fluids 2012;24:015103.
[51] Walters D, Bhushan S, Alam M, Thompson D. Investigating of a dynamic hybrid RANS/LES modelling methodology for finite-volume CFD simulations. Flow Turbul Combust 2013;91:643–67.
[52] Verma A, Park N, Mahesh K. A hybrid subgrid-scale model constrained by Reynolds stress. Phys Fluids 2013;25:110805.
[53] Chen S, Xia Z, Pei S, Wang J, Yang Y, Xiao Z, Shi Y. Reynolds-stress-constrained large-eddy simulation of wall-bounded turbulent flows. J Fluids Mech 2012;703:1–28.
[54] Cahuzac A, Boudet J, Borgnat P, Lévêque E. Smoothing algorithms for mean-flow extraction in large-eddy simulationof complex turbulent flows. Phys Fluids 2012;24:015103.
[55] Hoyas S, Jiménez J. Reynolds number effects on the Reynolds-stress budgets in turbulent channels. Phys Fluids 2008;20(10):101511.
[56] Sagaut P, Deck S, Terracol M. Multiscale and multiresolution approaches in turbulence - LES, DES and hybrid RANS/LES methods: Applications and guidelines. 2nd ed.. Imperial College Press; 2013.
[57] Larsson J, Kawai S, Bodart J, Bermejo-Moreno I. Large eddy simulation with modeled wall-stress: recent progress and future directions. Mech Eng Rev 2016;3:15–00418.
[58] Murayama M, Nakakita K, Yamamoto K, Ura H, Ito Y, Choudhari MM. Experimental study on slat noise from 30P30N three-element high-lift airfoil at JAXA hard-wall lowspeed wind tunnel. In: 20th AIAA/CEAS aeroacoustics conference. 2014.
[59] Pascioni K, Cattafesta LN, Choudhari MM. An experimental investigation of the 30P30N multi-element high-lift airfoil. In: 20th AIAA/CEAS aeroacoustics conference. 2014.
[60] Ashton N, West A, Mendonça F. Flow dynamics past a 30P30N three-element airfoil using improved delayed detached-eddy simulation. AIAA J 2016.
[61] Choudhari MM, Lockard DP. Assessment of slat noise predictions for 30P30N high-lift configuration from BANC-III workshop. In: 21st AIAA/CEAS aeroacoustics conference. 2015.
[62] Pascioni KA, Cattafesta LN. Aeroacoustic measurements of leading-edge slat noise. In: 22nd AIAA/CEAS aeroacoustics conference (37th AIAA aeroacoustics conference). 2015.
[63] Zhang Y, Chen H, Wang K, Wang M. Aeroacoustic prediction of a multi-element airfoil using wall-modeled large-eddy simulation. AIAA J 2017;55(12).
[64] Klausmeyer SM, Lin JC. Comparative results from a CFD challenge over a 2D three-element high-lift airfoil. In: NASA technical momorandum 112858. 1997.